COMPUTER SIMULATION OF INTERGRANULAR STRESS CORROSION CRACKING VIA HYDROGEN EMBRITTLEMENT

Richard Whiting Smith
Bettis Atomic Power Laboratory
Bechtel Bettis Inc.
West Mifflin, PA 15122

DE-AC11-98PN38206

NOTICE

BETTIS ATOMIC POWER LABORATORY WEST MIFFLIN, PENNSYLVANIA 15122-0079

Operated for the U.S. Department of Energy
by Bechtel Bettis, Inc.

DISCLAIMER

DISCLAIMER

Portions of this document may be illegible in electronic image products. Images are produced from the best available original document.

Abstract

Computer simulation has been applied to the investigation of intergranular stress corrosion cracking in Ni-based alloys based on a hydrogen embrittlement mechanism. The simulation employs computational modules that address (a) transport and reactions of aqueous species giving rise to hydrogen generation at the liquid-metal interface, (b) solid state transport of hydrogen via intergranular and transgranular diffusion pathways, and (c) fracture due to the embrittlement of metallic bonds by hydrogen. A key focus of the computational model development has been the role of materials microstructure (precipitate particles and grain boundaries) on hydrogen transport and embrittlement. Simulation results reveal that intergranular fracture is enhanced as grain boundaries are weakened and that microstructures with grains elongated perpendicular to the stress axis are more susceptible to cracking. The presence of intergranular precipitates may be expected to either enhance or impede cracking depending on the relative distribution of hydrogen between the grain boundaries and the precipitate-matrix interfaces. Calculations of hydrogen outgassing and ingassing demonstrate a strong effect of charging method on the fracture behavior.

1.0 Introduction

Stress corrosion cracking (SCC) is the synergism of mechanical stress and chemical attack resulting in crack propagation in a susceptible material. Although SCC was first observed nearly 100 years ago [1], the mechanisms by which it operates are still under dispute. In the case of Ni-based alloys, such as alloys 600 and 690, three basic mechanisms have been postulated. The first, film rupture dissolution [2], postulates that creep in the metal leads to strains that fracture the passive oxide film on the alloy surface allowing rapid metallic corrosion to proceed into the material along grain boundaries until such time as the passive film reforms and the cycle repeats. The second, internal oxidation [3], assumes that environmental oxygen, having diffused along grain boundaries to the interior of the alloy, combines with fresh metal to produce a brittle oxide, the formation of which results in lattice mismatch strains that fracture the grain boundaries. The third, hydrogen embrittlement [4], is thought to occur when hydrogen, produced by corrosion reactions on the metal-liquid interface of the alloy, enters the material and concentrates at grain boundaries to either induce grain boundary decohesion [5] or locally enhanced plasticity [6].

In order to differentiate between these mechanisms and to determine the environmental regimes under which they may operate, it is necessary to have detailed models describing their operation. Toward that end, efforts have been directed at the development of a computational tool capable of simulating the various processes and mechanisms contributing to SCC. The effort has been focussed on hydrogen embrittlement as the fundamental cause of cracking.

This paper describes the computational methods employed thus far in modeling SCC and presents the results of several numerical simulations completed to date. The emphasis here is on the mechanical and metallurgical aspects of the problem.

2.0 Method

2.1 Basic Model Overview

The computational package developed to study SCC consists of three main modules for the treatment of electrochemistry, solid state hydrogen diffusion and finally, deformation and fracture. The electrochemistry module addresses the transport of chemical species within the aqueous environment in and around a crack or crevice in a wetted metal. This module computes the rate at which various electrochemical reactions (e.g. metal dissolution and hydrogen generation) proceed as a function of position along the solid-liquid interface. The solid state transport module tracks the time evolution of hydrogen in the material due to spatial gradients in concentration as well as trapping and diffusion through grains and along grain boundaries. The fracture module computes the local degradation of mechanical properties due to the hydrogen distribution and predicts the spatial dependence of the formation and propagation of cracks during the deformation simulation.

2.2 The Electrochemistry Module

The electrochemical module of the simulation treats the transport of chemical species in the aqueous solution in and around an idealized stress corrosion crack, and computes the rates with which various electrochemical reactions take place at various positions along the solid-liquid interface. Solution to the electrochemical model, to be described in this publication, yields hydrogen concentrations and hydrogen generation rates that can be used as boundary conditions for the solid state transport module.

2.3 Model Geometry for Solid Transport and Fracture Modules

As described below, both the solid state transport and the fracture modules employ a discrete 2-dimensional finite difference spatial model containing a simulated microstructure. Grain boundaries and precipitate particles are included in the model by partitioning the network of discrete nodes into various regions corresponding to distinct grains and phases (Fig. 1). The effect of microstructure on materials behavior is included by tailoring the form of internodal bonds (used to describe local mechanical and transport properties) that connect neighboring nodes to reflect the local behavior at each point in space. Simulated polycrystalline microstructures are obtained by applying a stochastic grain growth algorithm to a randomly generated fine grain structure superimposed onto the discrete nodal lattice. The growth algorithm, based on an application of the Metropolis Monte Carlo method and the Potts model made popular by Srolovitz et al. [7-11], treats the motion of individual grain boundary segments on a discrete lattice (Fig. 1) which move in such a way as to reduce the total energy of the system toward a minimum with increasing time. For the case of normal grain growth considered here, the total energy of the system is simply proportional to the total grain boundary area.

Because grain orientation with respect to the direction of crack propagation has recently been identified as a significant factor in controlling SCC crack growth rate [12], it is important to be able to address issues related to the orientation of elongated grains. A preference in the shape of grains with respect to an arbitrary axis is accomplished by applying an affine transformation to produce a homogeneous deformation of the nodal lattice. The grain numbers from the deformed structure may then be mapped onto an undeformed lattice to produce a model with modified microstructure. An application of this sort of deformation is appropriate in the case of thermomechanical treatments such as rolling, that tend to produce grains that are elongated in a given direction.

While the Monte Carlo scheme is sufficient to treat the growth of metallic grains, it does not allow a direct simulation of the nucleation and growth of precipitate particles such as $M_{23}C_6$. These carbides, thought to play a significant role in SCC [13], form via a process of discontinuous precipitation [14] that requires the long range

transport of both chromium and carbon within the matrix and along the grain boundaries in Ni-based alloys. Precipitates of this form are included in the microstructure via an interactive graphical editor.

2.3 The Solid State Diffusion Module

The purpose of the solid state diffusion module is to calculate the time dependent hydrogen profile within the material. The transport simulation accounts for diffusion due to concentration gradients, including differences in diffusivities along intergranular and transgranular pathways. Trapping of hydrogen at saturable sinks is also considered. The elastic interaction between hydrogen and the internal stress field is currently being addressed but is not reported here. Hydrogen transport within the material is described in terms of a particle balance equation at each node of the finite difference mesh.

In order to account for traps lying in the space covered by some of the nodes and for the possibility that the traps are connects (eg. grain boundaries), the model actually calculates *two* interrelated concentrations at each node. The first is the average concentration expected to exist within the matrix region of a given node (that portion of the node comprised of perfect material) and the second is the concentration expected to exist at any traps (grain boundary or surface) that may lie within the node. The use of two concentration values per node allows consideration of the fact that only a small fraction of the nodal volume may represent strong traps (or regions of enhanced diffusivity) and presents a means to compute both local and volumetrically averaged quantities. A schematic illustration of the particle current exchanged between two adjacent nodes in this method is given in Fig. 2. Within the node, current flows between the matrix and trap regions, and between the nodes currents flow along pathways connecting matrix to matrix and trap to trap regions. The binding and transport properties assigned to each region and pathway are adjusted to reflect the heterogeneous structure of the material. For example, if one of the nodes in the pair contains no traps then the binding energy in its trap region is set to zero, forcing this region to look exactly like the matrix. The parallel pathways connecting the matrix to matrix and trap to trap regions of the nodes is used to reflect the parallel operation of bulk and grain boundary (or surface) transport that must exist between to adjacent nodes lying along a common boundary or surface. If the two trap regions are not connected by a fast pathway (they do not lie along a *common* boundary or surface) then the

diffusivity of the trap to trap connection can be assigned to the matrix value to reflect the fact that the traps are isolated from each other by some amount of bulk material. The equations for the particle concentrations at each node in this scheme are,

$$\frac{\partial C_i^M(t)}{\partial t} = \frac{1}{V_i^M}\left(\sum_j J_{ji}^{MM}(t) + J_i^{TM}(t)\right)$$

$$\frac{\partial C_i^T(t)}{\partial t} = \frac{1}{V_i^T}\left(\sum_j J_{ji}^{TT}(t) - J_i^{TM}(t)\right),$$

where C^T and C^M are the concentrations in the trap and matrix regions, V^T and V^M are the volumes of the trap and matrix regions, J^{TM} is the flow rate from the trap to the matrix region of a given node, J^{TT} is the trap to trap flow rate between nodes and J^{MM} is the matrix to matrix flow rate between nodes. Each of these flow rates is described in terms of the concentrations and binding energies in the various regions and the appropriate diffusion coefficient for matrix to matrix, trap to trap or trap to matrix transport,

$$J_{ji} = J_{j\to i} - J_{i\to j} = \nu\left(N_j e^{\frac{-E_{ji}}{kT}} - N_i e^{\frac{-E_{ij}}{kT}}\right),$$

where ν is the frequency with which jumps are attempted by each atom, N_i and N_j are the number of atoms at nodes i and j, E_{ji} is the energy barrier that must be overcome in jumping from site j to i, E_{ij} is the barrier height that must be overcome in jumping from i to j, and kT is thermal energy.

Because some of the traps in the system, notably the carbides, are quite strong, the model must account for the saturation of traps as the local concentration of vacant interstitial sites is depleted. This is accomplished by amending the equation for the rate at which particles jump from one node to the next. If the target node does not possess a saturation limit, this rate is given by the product of the concentration (expressed as atomic fraction) of

particles in the source node, C_i, the frequency with which each particle attempts a jump, ν, and the probability that any given jump will be successful, $p = exp(-E_{ij}/kT)$. If the target node saturates, then the jump rate must be modified to include the probability of finding an empty interstitial site in this node. For a saturation concentration of unity (one interstitial site per lattice site), this probability is $(1-C_j)$, giving a jump rate from i to j of

$$J_{ij} = \nu C_i e^{\left(\frac{-E_{ij}}{kT}\right)}(1-C_j).$$

Once the concentration in the target node, C_j, reaches the saturation limit, no further influx of particles is possible.

2.4 The Mechanical Response and Crack Propagation Module

The mechanical response and crack propagation module is used to compute the mechanical behavior of the finite difference mesh following application of external constraints placed on the system to represent stress and or strain. The response is described by the displacement in the positions of the mesh nodes due to the net forces placed on each node by its neighbors (plasticity is not yet considered). This type of model has been used previously to investigate cracking in laminated, particle reinforced and fiber reinforced alloys and composites [15,16], to simulate brittle fracture in single crystal and polycrystalline ceramics subjected to impact loading [17-19], and recently to study intergranular failure in gallium embrittled aluminum [20].

Net forces are determined from an internodal interaction energy expressed for each pair of neighboring nodes by a modified Lennard-Jones potential function,

$$\Phi(r) = \varepsilon\left(1+\left(\frac{R_0}{R}\right)^{12} - \left(\frac{R_0}{R}\right)^{6}\right).$$

This equation produces a minimum in potential energy (zero) at an equilibrium separation distance of R_o, and an increase in energy as the internodal separation, R, is either increased (tension) or decreased (compression) from this value. Due to the difference in exponents, 6 for tension and 12 for compression, the energy increases faster when nodes are compressed than extended. For very small displacements, the energy vs. distance relationship is

approximately harmonic. Because the purpose of the calculation is to simulate fracture, it is necessary to apply a cutoff to the Lennard-Jones function to account for the fact that the material fails irreversibly if strained too far. As shown in Fig. 3, bonds break if stretched in tension beyond a critical extension limit. At this point the bond loses its ability to support a load in tension, but retains its resistance to compression. The failure of bonds corresponds to the nucleation and growth of cracks in the continuous material. A cracking simulation is performed by applying a load or displacement to the finite mesh and then solving the mechanics equations describing the position each node adopts in response to the forces placed on it by its neighbors. Crack morphology is studied by determining the location of failed bonds.

In order to reflect the heterogeneous nature of the polycrystalline material, different characteristics are applied to internodal bonds in different regions of the sample. For example, bonds spanning grain boundaries can be embrittled by reducing the length to which these bonds can stretch before breaking. As described below, the effect of local chemistry, such as hydrogen content, can be included by specifying a functional relationship between the local concentration and the bond extension limit.

The fracture simulations are conducted by solving a system of equations for the motion of each mesh node due to the forces placed on it by its neighbors. This is done in accordance with boundary conditions describing the stress or strain applied to the sample. The present investigation is conducted using a constant strain rate applied in the y-direction. The equations of motion are solved using a damped dynamic integration method. The method is essentially that of a molecular dynamics calculation in which all nodes are attached to a thermostat set at 0K. The thermostat dampens out elastic waves that result from the snapping of bonds [17]. An alternative approach that may be more accurate, but is certainly more compute intensive is to step through a series of strain increments and at each step, iteratively perform an energy minimization procedure followed by the snapping of any bonds stretched beyond their limits [15].

3.0 Results and Discussion

3.1 Solid State Diffusion Simulations

The solid state diffusion module was used to study the transport of hydrogen in polycrystalline meshes representing materials containing the following: (1) clean grain boundaries, (2) intergranular carbide precipitates, (3) intergranular and transgranular carbide precipitates. The calculations were designed to simulate the redistribution of hydrogen upon low temperature aging following a high temperature gaseous charge. Additional calculations addressing the diffusion of hydrogen across sample surfaces were also performed.

The redistribution simulations were performed by first assigning a uniform hydrogen concentration of 220 appm to each node of the sample (charging) and then allowing the hydrogen to redistribute itself to the grain boundaries and precipitates at an aging temperature of 253K. The total aging time was taken as $3x10^4$ seconds (8.3 hrs) to assure the system attained near equilibrium conditions. The diffusion coefficients and binding energies used are given in Table I. As discussed in section 3.2, the aged samples were then subjected to fracture simulations in order to asses the effect of hydrogen redistribution.

3.1.1 Segregation to Precipitate-Free Grain Boundaries

Two polycrystalline samples were constructed with the Monte Carlo grain growth module, and then charged and aged as describe above. Figure 4 presents the average grain boundary hydrogen concentration as a function of aging time for one of the clean grain boundary samples. As expected, the concentration increases with time from its initial value to an equilibrium level determined by the grain boundary binding energy and aging temperature. The rate at which equilibrium is approached is governed by the diffusivity of the pathway connecting the boundaries (traps) to the matrix regions of the nodes. As described by Lassila and Birnbaum [21], the equilibrium bulk concentration at the grain boundary is given by

$$\frac{C_B}{1-C_B} = \left(\frac{C_H}{1-C_H}\right)\exp\left(\frac{-E}{kT}\right)$$

where C_B and C_H are the grain boundary and matrix hydrogen concentration, E is the binding energy of hydrogen to the boundary and kT is thermal energy. The approach to equilibrium can be approximated by the expression [21]

$$\frac{C_B(t)-C_0}{C_B-C_0}=1-\exp(\frac{-t}{\tau})erfc(\sqrt{\frac{t}{\tau}})$$

where C_0 is the initial concentration and τ is a time constant dependent on the diffusivity and length of the diffusion path.

3.1.2 Segregation to Intergranular and Transgranular Precipitates

A more interesting calculation, which is not so readily accessible by a simple analysis, is the redistribution of hydrogen in the presence of randomly distributed intergranular and transgranular precipitates. For these simulations, the polycrystalline meshes used in the previous calculations were edited to insert the precipitates. Two samples were constructed with only intergranular carbides. Two more were generated by adding transgranular carbides as well. In all samples, each carbide was represented by a single node in the mesh. Figure 5 displays the equilibrium concentration of hydrogen at each node in one of the samples containing both intergranular and transgranular carbide particles. An intermediate level of H (about 10^5 appm) is attained at the grain boundaries. A higher level (approaching 10^6 appm – complete saturation) is found at the interfaces to the precipitates. Due to the large binding energy of hydrogen to the precipitates, it is important to utilize a calculation that accounts for the saturability of the traps. Without this feature, the concentration in these regions would increase to physically unrealistic levels.

Figure 6 presents the time dependence of the hydrogen concentration at grain boundary nodes (that do not lie immediately adjacent to carbides) and precipitate nodes for a sample containing grain boundaries and intergranular precipitates. While the concentration at both node types increases rapidly with time, it is seen that the grain boundary content does not increase as quickly as it does in the precipitate free case (Fig. 4). Figure 7 compares the time evolution of the grain boundary hydrogen concentration for samples with and without

, intergranular precipitates. The reduction in hydrogen observed at *clean sections* of boundary when precipitates are present results from the fact that the carbides (stronger sinks) are connected to the grain boundaries and are therefore able to drain them of their hydrogen. As the precipitate nodes approach their saturation level, the rate at which they absorb hydrogen from the boundaries is reduced and the boundary hydrogen level starts to increase due to influx from the matrix material. The grain boundary hydrogen level is suppressed until the grain boundary precipitate particles become saturated.

The observed influence of the intergranular carbides on the grain boundary hydrogen level raises two interesting questions. The first is whether or not the judicious placement of precipitates could act as hydrogen traps and therefore reduce the susceptibility of a material to hydrogen embrittlement. The answer to this question may depend on whether or not hydrogen adversely affects the mechanical properties of the precipitates, but even if these interfaces are also embrittled, it may be possible to strengthen the overall material, by spacing the particles in a way that the embrittled interfaces are isolated from each other by reasonably long stretches of boundaries that have been denuded of hydrogen and therefore considerably strengthened. This question is addressed in more detail in section 3.2.2.

3.1.3 Communication of Hydrogen between Sample and Environment

The second question motivated by the simulation results concerns possible differences in mechanical behavior between pre-charged samples and those that are loaded in-situ during either gaseous or cathodic charging. In the first case, the hydrogen moves to the boundary from the matrix material, but also may escape the sample by outgassing through free surfaces. Outgassing, which was not considered in the diffusion calculations described earlier in this section, may not only lower the overall hydrogen concentration in the material but also give rise to a significant difference in the concentrations at the surface and interior of the sample before equilibrium is achieved. During in-situ charging, hydrogen must enter the material at a free surface and then diffuse to its interior along matrix and grain boundary pathways. Prior to the establishment of equilibrium, this condition may lead to a substantial hydrogen gradient with concentrations near the surface much higher than those in the interior. Symons [22] has recently conducted an experimental investigation into this issue and determined that

in-situ charging appears to produce fracture at lower stress intensities than those needed for pre-charged samples. His explanation is that higher grain boundary hydrogen concentrations can be produced within the first several microns of the in-situ samples at short times due to contact with the environment. These higher surface levels produce fracture which allows the exposed surface to advance into the material, allowing the next layer to attain a high hydrogen concentration in an equally short time increment. In contrast, the hydrogen levels near the crack tip of the pre-charged samples are expected to be low due to outgassing and therefore less likely to promote crack advance. In these samples, cracking appears to begin at some distance away from the surface into the material.

In order to test this idea, simulations were performed on polycrystalline samples in the absence of carbides. One sample was charged to a bulk concentration of 3650 appm and aged for $3x10^4$ second (8.3 hours) at 54 °C. Boundary conditions were established such that hydrogen was allowed to leave the sample through one surface connected to a hydrogen free environment. The second was exposed, from an initially hydrogen free state, to an external environment containing a hydrogen pressure such that the equilibrium bulk concentration in the material would also be 3650 appm at 54 °C. The concentration of hydrogen on the grain boundaries was monitored as a function of time and position across the samples. Figure 8 presents the time evolution of grain boundary hydrogen for both simulations. As proposed by Symons, the concentration near the surface of the in-situ sample increases rapidly while the interior concentration remains low. In stark contrast, the concentration in the surface layer of the pre-charged sample is significantly reduced by outgassing. The plots clearly show that at the times at which the laboratory samples were fractured (between 1 and 10 hours), the concentration at the inside of the material is considerably different than in the surface layer. Because the samples have substantially different hydrogen profiles, they display significantly different crack advance behavior, as described in section 3.2.3.

3.2 Crack Propagation Simulations

3.2.1 Effect of Grain Boundary Strength and Grain Orientation

Fracture simulations were conducted, using the damped dynamic integration method, to assess the effect of grain boundary strength and grain orientation on the fracture characteristics of polycrystalline finite meshed samples. The simulations using variable grain boundary strength were performed in order to determine the relationship between relative embrittlement and the observed amount of intergranular (IG) fracture. The simulations performed with variable grain orientation (elongated grains) were motivated by recent experimental results of Moshier and Brown [12] demonstrating that SCC crack growth rates depend strongly on the orientation of the propagating crack with respect to the rolling direction in rolled material.

For the grain boundary strength simulations, two polycrystalline finite mesh samples each containing 28299 nodes were employed. In each case, an equiaxed grain structure was constructed using the Potts model grain growth simulator with a randomly selected seed. The thickness of the samples in the direction of crack propagation is 150 nodes (1144.5 μm) and the average grain size is 25 nodes (190 μm). Prior to the fracture simulations, a small crack was initiated on the surface of each sample at a grain boundary by removing three nodes from the mesh. Fracture simulations were conducted on samples A and B with the relative strength (defined as the elongation to fracture) of all grain boundary nodes set to a given fraction of the matrix node strength. Runs were made with grain boundary strengths of 20%, 40%, 60%, 80% and 100% of the matrix value.

In order to investigate the influence of grain boundary orientation with respect to the direction of crack propagation, copies of samples A and B were "rolled" so as to produce grains that were elongated by a factor of 3 to 1 either perpendicular (samples Ay and By) or parallel (samples Ax and Bx) to this direction. After being notched to remove three grain boundary nodes at the surface, the elongated samples were subjected to fracture simulations with relative grain boundary strengths set at 20%, 40%, 60% and 80% of the matrix value. A detailed list of simulation parameters used in these calculations is given in Table II.

Figure 9 presents the fraction of the crack path passing along the grain boundaries as a function of relative grain boundary strength for the equiaxed and elongated samples. In each case, it is clear that the extent to which cracks follow the grain boundaries increases as the relative grain boundary strength (by whatever means) is reduced. In the case of the equiaxed samples, the fraction of intergranular fracture increases in a fairly linear fashion with decreasing grain boundary strength, producing nearly 100% IG failure once the boundary bond elongation limit is reduced to 20% of the matrix. In comparison, a previous investigation of impact induced fracture of a similar material system [18] suggested that 100% IG failure was achieved with even stronger boundaries (40%), but in this case, elastic waves of compression and rarification following a sudden impact were free to travel throughout the system in all directions after having been reflected from free surfaces. Because of these reflections, the relative orientation of the boundaries to the initial applied load was insignificant. In the present case of uniform extension, weak boundaries do not fracture unless properly oriented with respect to the applied load, and as a result, the fractional strength at which nearly complete IG fracture occurs is reduced. The crack paths for the equiaxed sample A is shown in Fig. 10 for relative grain boundary strengths of 20% and 80%, clearly illustrating the shift from transgranular to intergranular fracture with decreasing boundary cohesion.

The effect of the relative orientation of grain boundaries and applied load is also illustrated in Fig. 9 by the results of the elongated samples. At a given level of boundary strength, samples with grains elongated parallel to the crack clearly show more IG fracture than the equiaxed specimens, and samples with grains elongated perpendicular to the crack clearly show less. The orientation effect is most pronounced at the intermediate strength levels, and diminishes when the boundaries become as strong as the matrix or when they are made incredibly weak. For a boundary strength (maximum bond elongation) of 60%, the orientation effect is shown in Fig. 11, where the degree of IG fracture increases from 30% (perpendicular) to 45% (equiaxed) to 70% (parallel). This trend is consistent with the Moshier and Brown results [12], revealing that SCC cracks propagate faster when oriented in a direction parallel to rolling (and therefore grain elongation). For 60% grain

boundary strength, the effect of orientation on crack morphology is illustrated in Fig. 12, demonstrating the shift from intergranular to transgranular fracture as the boundaries are oriented away from the crack path.

As an additional measure of the crack propagation behavior, Fig. 13 shows the time to failure (a through thickness crack) as a function of relative grain boundary strength for each of the equiaxed and elongated samples. As expected, in each case, the time to failure decreases as the boundaries are weakened. The parallel orientation is slightly more susceptible to lifetime reduction with decreasing strength and the perpendicular orientation seems significantly more resistant. As with the IG fraction measurement, the effect is most pronounced at intermediate boundary strengths, but the largest effect is seen at a strength of 40% rather than 60%. The limited number of simulations performed in this study prevents a detailed analysis of this point.

Because the cracks advance preferentially along the weaker pathways, it is possible for them to become arrested when they move into a region of microstructure where the weakest path (the grain boundary) is not oriented parallel to the direction of propagation. Because the strain in the early stages of these simulations is too low to force a crack through the matrix material, the crack must either be arrested or diverted into a direction in which its forward travel is slowed. An example of this is shown in Fig. 14, where a crack, initially propagating quickly, has slowed because the grain boundary has turned away from the foraward direction. Although the grain boundary is still weak, it is oriented more parallel to the direction of loading and therefore the component of strain resolved along the intergranular bonds is very small, and the bonds do not exceed their critical extension limits. In the brittle fracture simulations conducted here, the main effect of a given type of microstructure appears to be its propensity (or lack thereof) to place obstructions in the direction of easy propagation or to orient these weak pathways such that an applied load does not open the crack effectively.

3.2.2 Effect of Intergranular and Transgranular Carbide Precipitates

In order to investigate the effect of carbides on hydrogen induced fracture, simulations were performed on samples containing clean boundaries, intergranular precipitates, and a combination of intergranular and transgranular precipitates. The samples were charged with hydrogen as described in section 3.1, and then

fractured via the quasi-dynamic integration method. The influence of hydrogen on local mechanical properties was modeled by assuming that the critical extension at which any bond fractures is given by

$$\varepsilon = \varepsilon_o - \beta(1 - \exp(-\alpha(H - H_0)),$$

where H is the local hydrogen content, H_0 is a threshold level below which no hydrogen effect is perceived, ε_o is the critical extension in the absence of hydrogen, and α and β are scaling constants. We take ε_o=β=0.05, H_o=0.035 (fractional site occupancy), and α=24.76. As such, the critical extension decreases from 0.05 to 20% of this value as the local hydrogen content increases from 0.035 to 0.10. This behavior was selected to match the observations of Lassila and Birnbaum on hydrogen effects in Ni [21]. All bonds were assumed to follow the behavior prescribed by this function, no distinction being made between matrix and grain boundary bonds other than that arising solely due to differences in local hydrogen content. Additional efforts are underway to improve the bonds by incorporating results of quantum mechanical calculations of interface strengths into the analysis.

Results for the two clean grain boundary samples are given in Table III, which presents both the time to failure and the fraction of the crack running along grain boundaries as a function of grain boundary hydrogen. As expected, as the hydrogen level is increased, the time to failure decreases and the fraction of broken bonds falling along the grain boundaries increases.

Table IV presents results for samples containing intergranular precipitates. For a low hydrogen concentration at each sink (below the threshold), the material behaves almost exactly as do the samples without carbides. This results from the fact that all of the internodal bonds in the system are considered to be identical except for their elongation limit which is assumed to be a function only of the local hydrogen content. The validity of this assumption has not yet been assessed, but future experimental work or quantum chemical modeling can be used to determine if the bond function needs to be modified. When the hydrogen content is high at both sinks (following a long age to equilibrium), the fraction of IG fracture increases and the time to failure decreases. In comparison to the clean boundary, also at equilibrium, the time to failure is less and fraction IG fracture is greater. This results from the fact that the equilibrium hydrogen concentration at the metal-carbide interface is

, higher than that on the metal-metal grain boundary in the absence of carbides, promoting failure along these grain boundaries.

A more interesting situation arises when the carbide interfaces are loaded with a high hydrogen level, but the level at the metal-metal grain boundaries is held below the threshold. This case hasn't been taken from the aging simulations, but specifically constructed to help separate the direct effect of the integranular carbides on the local mechanical properties of the boundary from its effect on hydrogen level between the intergranular carbides. In these cases, the fraction of IG failure appears to fall between the "low-low" and "high-high" hydrogen extremes (Table IV), but examination of the fracture surfaces reveals that the crack is predominantly intragranular. In addition, it appears that in comparison to the clean grain boundary case with intermediate hydrogen level, the time to failure actually increases. As demonstrated in Fig. 15, by curves reporting the time evolution of the number of broken bonds, most of the carbide-metal bonds break early in the simulation due to high local hydrogen concentration. But then, because the hydrogen level in the metal-metal boundaries is low, the cracks to not continue to propagate until the sample is strained to a degree sufficient to activate a transgranular crack. Since the carbides in these samples are separated by sections of clean boundary (an arbitrary choice not always realized), the cracks nucleated at the carbide-metal interfaces do not link up. It appears that the carbides' tendency to drain the surrounding boundaries of hydrogen (if properly aged) may counteract their local degradation of the boundary and allow the overall structure to be more hydrogen resistant. This trade-off will obviously be strongly affected by the relative placement of the carbides and the thermal/charging history of the sample. This effect is confirmed for samples containing interface and grain boundary hydrogen contents taken at an intermediate time during an aging simulation. Fracture runs made on the samples described in section 3.1.2 (taken at 10^3 s, the time at which the depression in grain boundary hydrogen concentration due to the presence of intergranular carbides is greatest), are depicted in Fig. 16. As described above, small isolated cracks nucleate early at the carbide-metal interfaces, but then no crack growth is observed for quite some time. The onset of macroscopic crack propagation in this sample is delayed beyond the time at which considerable crack growth has been experienced by the sample containing only clean grain boundaries.

The behavior of the samples containing both intergranular and transgranular carbides is qualitatively similar to the cases containing only intergranular carbides (Table V).

3.2.3 Effect of Communication to the Environment

Section 3.1.3 focussed on hydrogen charging experiments conducted by Symons [22] and his belief that outgassing might be expected to denude the surfaces layers of hydrogen in such a way that prevented the propagation of cracks at small stresses and strains. The hypothesis concerning the hydrogen profile was confirmed by diffusion simulations, but no direct assessment of the effect of this hydrogen profile on cracking behavior can be made until fracture simulations are applied to the samples. In order to begin this assessment, crack growth simulations were run on two pre-charged and aged samples. The first, aged without outgassing to produce a uniform distribution of grain boundary hydrogen across the sample, and the second aged in a hydrogen free environment to produce the profile discussed in section 3.1.3. Constant extension rate simulations were conducted with the damped dynamic integration method. The time evolution of the number of broken bonds in each sample is shown in Fig. 17. Clearly fracture is delayed in the sample in which the surface hydrogen concentration (near the notch tip) is at the lower value due to outgassing. Once cracking begins, it propagates through each sample at roughly the same rate (the interiors of the samples are quite similar), but the delay in the *onset* of crack propagation from the surface notch seems directly related to the reduced concentration in grain boundary hydrogen. While these results seem qualitatively consistent with Symons' results and expectations, it must be pointed out that the mechanical boundary conditions employed in these simulations do not match those of a compact tension (CT) specimen. By virtue of their geometry CT's experience a more complex stress state than does a sample in uniaxial tension, one key difference being the existence of stress gradients in the CT. The mechanical module can be modified to impose a 2D analog to this case, but the work has not yet been undertaken. Because crack extension is very likely a strong function of both local stress and local hydrogen concentration, an accurate model of the each profile is necessary if an accurate simulation of a specific kind of test is desired.

4.0 Summary and Conclusions

A computer simulation package is being developed to model the various mechanisms contributing to SCC in Ni-based alloys. The simulation addresses electrochemical reactions, solid state hydrogen diffusion and fracture due to hydrogen embrittlement of both intra- and inter-granular bonds. One of the primary goals of the modeling effort is the explicit treatment of materials microstructure and the spatial arrangement of microstructural features. Preliminary transport simulations have demonstrated that due to the enhanced binding energy at precipitates and the greater mobility along grain boundaries, intergranular carbides may act to suppress hydrogen levels along clean sections of grain boundaries, but only while the precipitates are unsaturated. In addition, calculations of outgassing and ingassing show that hydrogen levels near a sample surface depend dramatically on the charging method. This result has important implications in the interpretation of hydrogen embrittlement experiments. Simulations of fracture demonstrate that intergranular fracture increases with grain boundary embrittlement and that grain orientation strongly influences the material's susceptibility to cracking. Prior to the saturation of hydrogen sites at precipitates, the presence of these particles might tend to supress cracking by drawing hydrogen away from sections of grain boundary. Saturated precipitates do not attract additional hydrogen and therefore would not be expected to mitigate cracking in this way (they might suppress it by electrochemical means if exposed to the aqueous environment). Fracture simulations conducted on samples possessing hydrogen profiles from different charging methods support Symons' contention that in situ charging accelerates cracking by producing high hydrogen levels near the surface of the material in the immediate vicinity of the crack tip.

References

1. R. H. Jones, **Stress Corrosion Cracking, Materials Performance and Evaluation**, ASM International, Materials Park, 1992.

2. D. A. Vermilyea, *J. Electrochem. Soc.* **119** (1972) 405.

3. P. M. Scott, M. Le Calvar, "Some Possible Mechanisms of Intergranular Stress Corrosion Cracking of Alloy 600 in PWR Primary Water", **6th Int. Symp. On Environmental Degradation of Materials in Nuclear Power Systems – Water Reactors**, Ed. R. E. Gold, E. P. Simonen, TMS, Warrendale 1993, p 657.

4. R. M. Latanision, "General Overview: Atomistics of Environmentally-Induced Fracture", **Atomistics of Fracture**, Ed. R. M. Latanision, J. R. Pickens, Plenum Press, New York, 1983, p 3.

5. E. A. Steigerwald, F. W. Schaller, A. R. Troiano, *Transactions of the Metallurgical Society of the AIME* **218** (1960) 832.

6. C. D. Beachem, *Met. Trans.* **3** (1972) 437.

7. M. P. Anderson, D. J. Srolovitz, G. S. Grest, P. S. Sahni, *Acta Metall.* **32** (1984) 783.

8. D. J. Srolovitz, M. P. Anderson, P. S. Sahni, G. S. Grest, *Acta Metall.* **32** (1984) 793.

9. D. J. Srolovitz, M. P. Anderson, G. S. Grest, P. S. Sahni, *Acta Metall.* **32** (1984) 1429.

10. G. S. Crest, D. J. Srolovitz, M. P. Anderson, *Acta Metall.* **33** (1985) 509.

11. D. J. Srolovitz, G. S. Grest, M. P. Anderson, *Acta Metall.* **33** (1985) 2233.

12. W.C. Moshier and C.M. Brown, "Effect of Cold Work and Processing Orientation on the SCC Behavior of Alloy 600," CORROSION/99, Paper 449, NACE, San Antonio, April 25-30, 1999.

13. H. A. Domian, R. E. Emanuelson, L. W. Sarver, G. J. Theus, L. Katz, *Corrosion,* **33** (1977) 26.

14. D. B. Williams, E. P. Butler, *International Review of Metals*, **3** (1981) 153.

15. W. H. Yang, D. J. Srolovitz, G. N. Hassold, M. P. Anderson, "Microstructural Effects in the Fracture of Brittle Materials", **Simulation and Theory of Evolving Microstructure**, Ed. M. P. Anderson, A. D. Rollett, The Metallurgical Society of AIME, 1990, p. 277.

16. R. Gibala, A. K. Ghosh, D. C. Van Aken, D. J. Srolovitz, A. Basu, H. Chang, D. P. Mason, W. Yang, *Materials Science and Engineering,* **A155** (1992) 147.

17. R. W. Smith, D. J. Srolovitz, *Modelling and Simulation in Materials Science and Engineering,* **2** (1994) 1153.

18. R. W. Smith, D. J. Srolovitz, *Modelling and Simulation in Materials Science and Engineering,* **3** (1995) 665.

19. R. W. Smith, D. J. Srolovitz, "Computer Simulation of Impact Induced Fracture and Fragmentation in Brittle Solids", **Shock Compression of Condensed Matter - 1995**, Ed. S. C. Schmidt, W. C. Tao, American Institute of Physics, Woodbury, 1996, p. 171.

20. M. Grah, K. Alzebdeh, P. Y. Sheng, M. D. Vaudin, K. J. Bowman, M. Ostoja-Starzewski, *Acta Mater.* **44** (1996) 4003.

21. D. H. Lassila, H. K. Birnbaum, *Acta Metall.* **34** (1986) 1237.

22. D. M. Symons, "A Comparison of Internal Hydrogen Embrittlement and Hydrogen Environment Embrittlement of X-750" submitted to Engineering Fracture Mechanics, available through DOE Office of Scientific and Technical Information, Oakridge, TN, as Bettis paper B-T-3256.

Table I

Diffusion Coefficients and Hydrogen Binding energies.

Parameter	Value
Diffusivity	$D = D_o \exp(-E/kT)$
Binding energy to matrix nodes	0.0 eV
Binding energy to metal-metal boundaries	-0.135 eV
Binding energy to metal-carbide boundaries	-0.270 eV
Matrix migration energy	0.41460 eV
Grain boundary migration energy	0.29635 eV

Table II

Parameters Used in Damped Integration Method

Internodal Distance, R_o	7.63 μm
Strain Rate	3×10^{-7} (-)/md step
Maximum Matrix Bond Extension	0.05 R_o
Damping Time Constant	20 md steps

Table III

Effect of Grain Boundary Hydrogen on Clean Boundaries

Grain Boundary H (fraction)	% IG Fracture	Time to Failure (10^3 steps)
0.03	6	80
0.07	58	54
0.10	85	37

Table IV

Effect of Hydrogen on Samples with Intergranular Carbides

GB H level PPT H level	% IG Fracture	Time to Failure (10^3 steps)
Low Low	8	80
Low High	69	71
High High	93	34

Table V

Effect of Hydrogen on Samples with Intergranular and Transgranular Carbides

GB H level PPT H level	% IG Fracture	Time to Failure (10^3 steps)
Low Low	10	80
Low High	79	72
High High	96	33

Figures

Fig. 1. A) Discretized region of material showing position of mesh nodes and nearest neighbor bond locations. Typical samples for use in the mechanics module possess on the order of 20 thousand nodes. (B) Sample microstructure (grain boundary network) superimposed onto section of the discrete node network. Bonds connecting nodes inside different regions or spanning the interface between regions may be assigned different mechanical properties to reflect the heterogeneous nature of the material.

Fig. 2. Schematic relation of neighboring nodes including various particle transport pathways. Within the nodes, particles flow between the matrix region and trap region. Between the nodes, particles flow via parallel pathways connecting matrix to matrix regions and trap to trap regions.

Fig. 3. Non-linear internodal interaction potential for nearest neighbor bonds. The standard Lennard-Jones 6-12 potential is truncated on the tensile side at a cutoff distance, beyond which the bond is considered to have snapped. Broken bonds maintain an ability to support load in compression but not in tension.

Fig. 4. Time evolution of grain boundary hydrogen content for a clean grain boundary during aging of pre-charged samples. The simulation is performed without outgassing.

Fig. 5. Equilibrium concentration of hydrogen at each node in one of the samples containing both intergranular and transgranular carbide particles. The darkest nodes represent grain boundary hydrogen content of about 10^6 appm. Grey represents a value near 10^5 appm.

Fig. 6. Time evolution of grain boundary hydrogen content (away from precipitates) and precipitate-matrix interface hydrogen content for sample containing intergranular precipitates.

Fig. 7. Time evolution of the ratio of grain boundary hydrogen content for samples in the presence and absence of intergranular carbides. Carbides suppress the buildup of grain boundary hydrogen in these simulations.

Fig. 8. Time evolution of grain boundary hydrogen content for pre-charged sample and in-situ sample as a function of distance from the free surface. Each curve represents an average for a 50 μm wide slice.

Fig. 9. Fractional intergranular failure (number of broken grain boundary bonds / total number of broken bonds anywhere in the sample) as a function of relative grain boundary bond strength and grain elongation. Each point is averaged from 2 simulations.

Fig. 10a. Crack morphology at the end of the simulation for equiaxed sample A with 20% grain boundary bond strength. The crack path is largely intergranular.

Fig. 10b. Crack morphology at the end of the simulation for equiaxed sample A with 80% grain boundary bond strength. The crack path is largely transgranular.

Fig. 11. Fractional integranular failure (number of broken grain boundary bonds / total number of broken bonds anywhere in the sample) as a function of grain orientation for grain boundary bond strength of 60%.

Fig. 12a. Crack morphology at the end of the simulation for sample Ax (grains elongated parallel to crack propagation) with 60% grain boundary bond strength. The crack path is largely intergranular.

Fig. 12b. Crack morphology at the end of the simulation for sample A (equiaxed grains) with 60% grain boundary bond strength. The crack path is intergranular and transgranular.

Fig. 12c. Crack morphology at the end of the simulation for sample Ay (grains elongated perpendicular to crack propagation) with 60% grain boundary bond strength. The crack path is largely transgranular.

Fig. 13. Time to failure (crack extends across the entire thickness of the sample) as a function of relative grain boundary bond strength and grain elongation. Each point is averaged from 2 simulations.

Fig. 14. Portion of sample B finite mesh showing broken bonds at 22000 time steps. The crack has propagated in from the right and down the grain boundary, but halts temporarily as the boundary turns downward, taking the boundary bonds out of a high strain orientation.

Fig. 15. Time evolution of the number of broken bonds for sample containing intergranular carbides.

Fig. 16. Time evolution of the number of broken bonds for samples aged to 1000 seconds with and without intergranular carbides.

Fig. 17. Time evolution of the number of broken bonds for aged samples with and without surface outgassing.

(a)

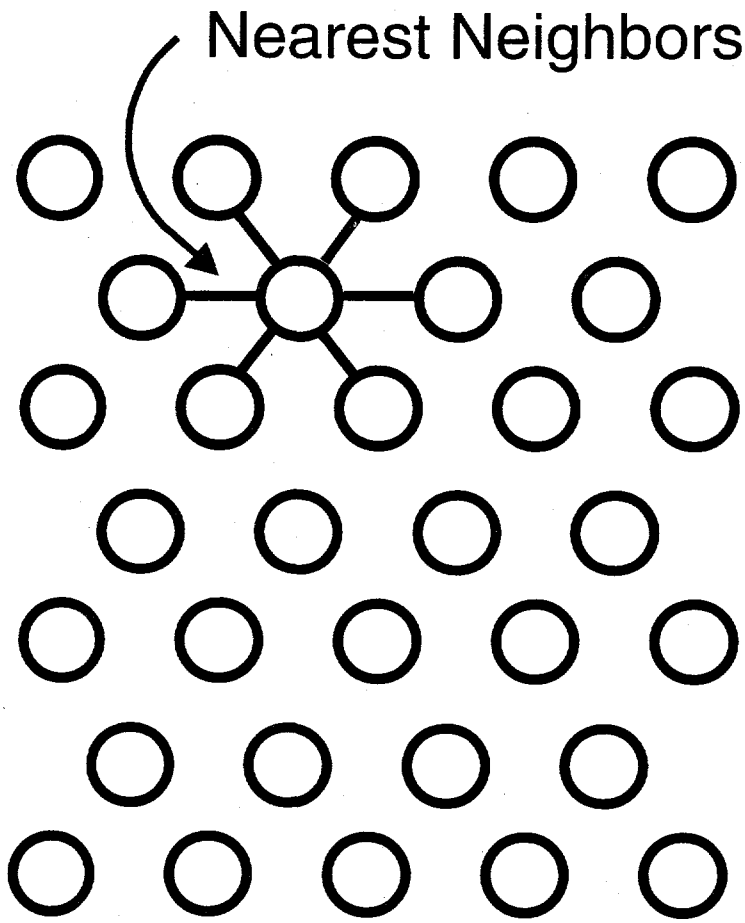

Fig. 1a. Discretized region of material showing position of mesh nodes and nearest neighbor bond locations. Typical samples for use in the mechanics module possess on the order of 20 thousand nodes.

(b)

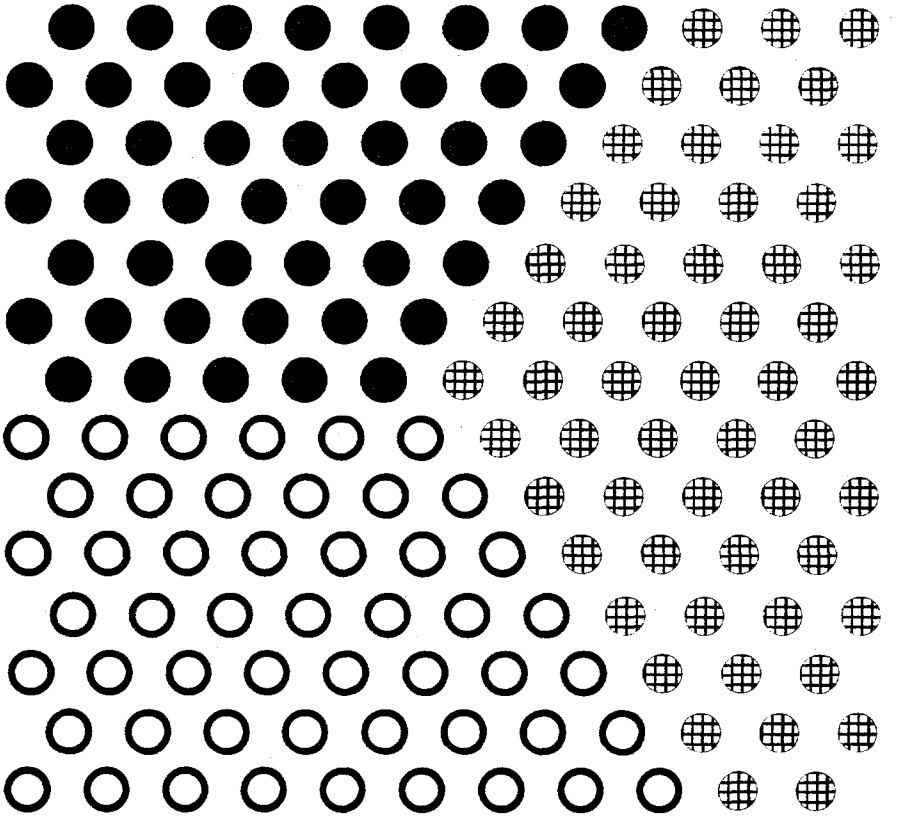

Fig. 1b. Sample microstructure (grain boundary network) superimposed onto section of the discrete node network. Bonds connecting nodes inside different regions or spanning the interface between regions may be assigned different mechanical properties to reflect the heterogeneous nature of the material.

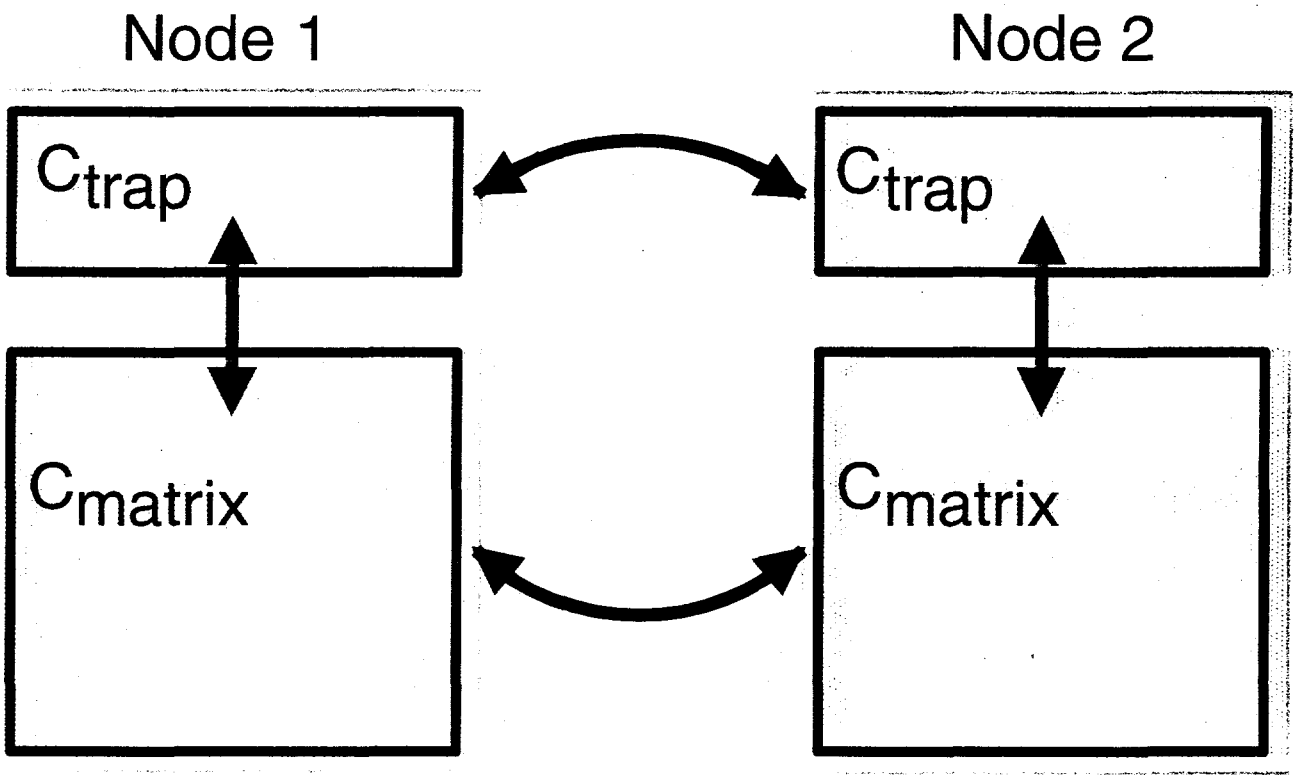

Fig. 2. Schematic relation of neighboring nodes including various particle transport pathways. Within the nodes, particles flow between the matrix region and trap region. Between the nodes, particles flow via parallel pathways connecting matrix to matrix regions and trap to trap regions.

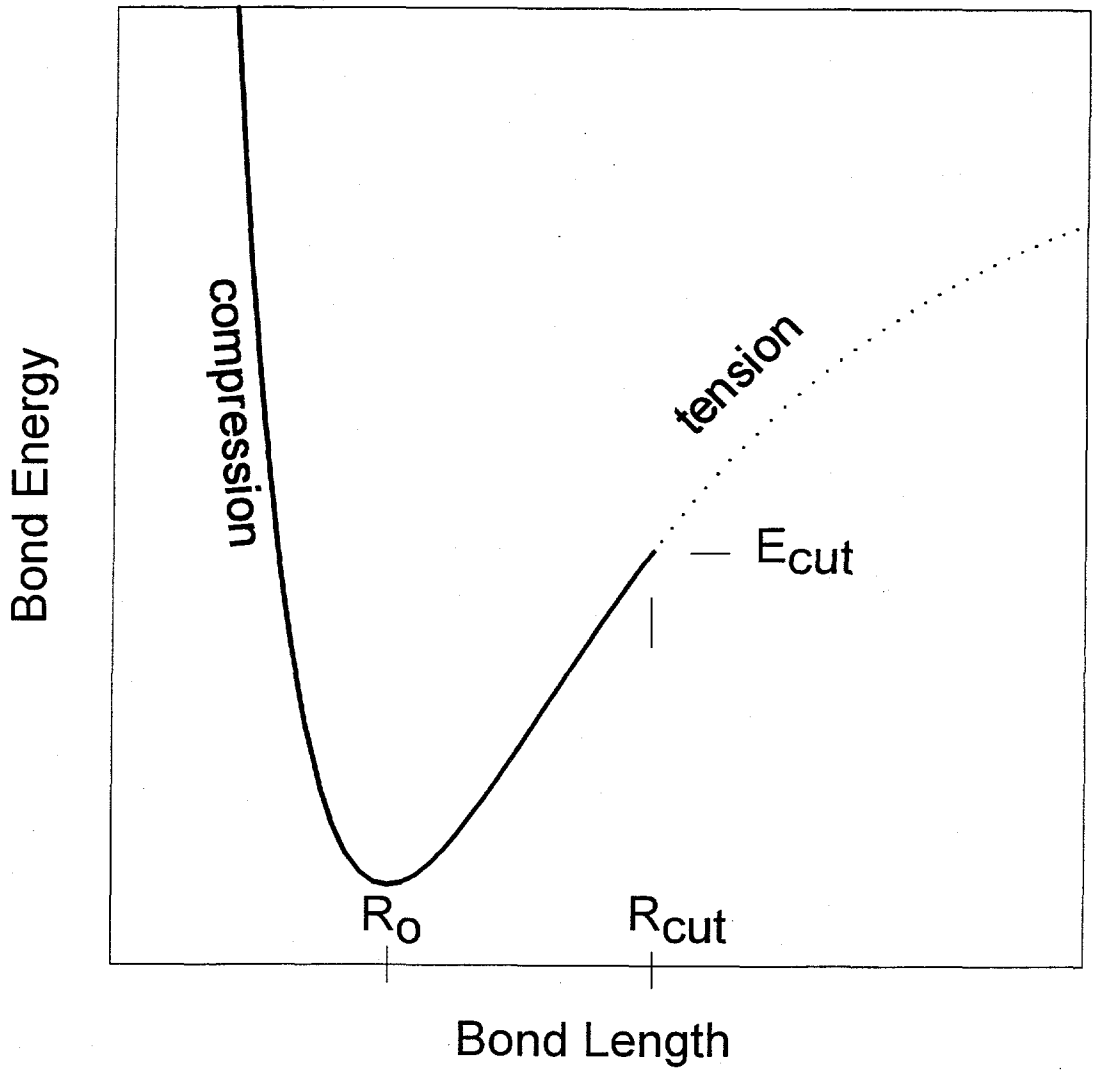

Fig. 3. Non-linear internodal interaction potential for nearest neighbor bonds. The standard Lennard-Jones 6-12 potential is truncated on the tensile side at a cutoff distance, beyond which the bond is considered to have snapped. Broken bonds maintain an ability to support load in compression but not in tension.

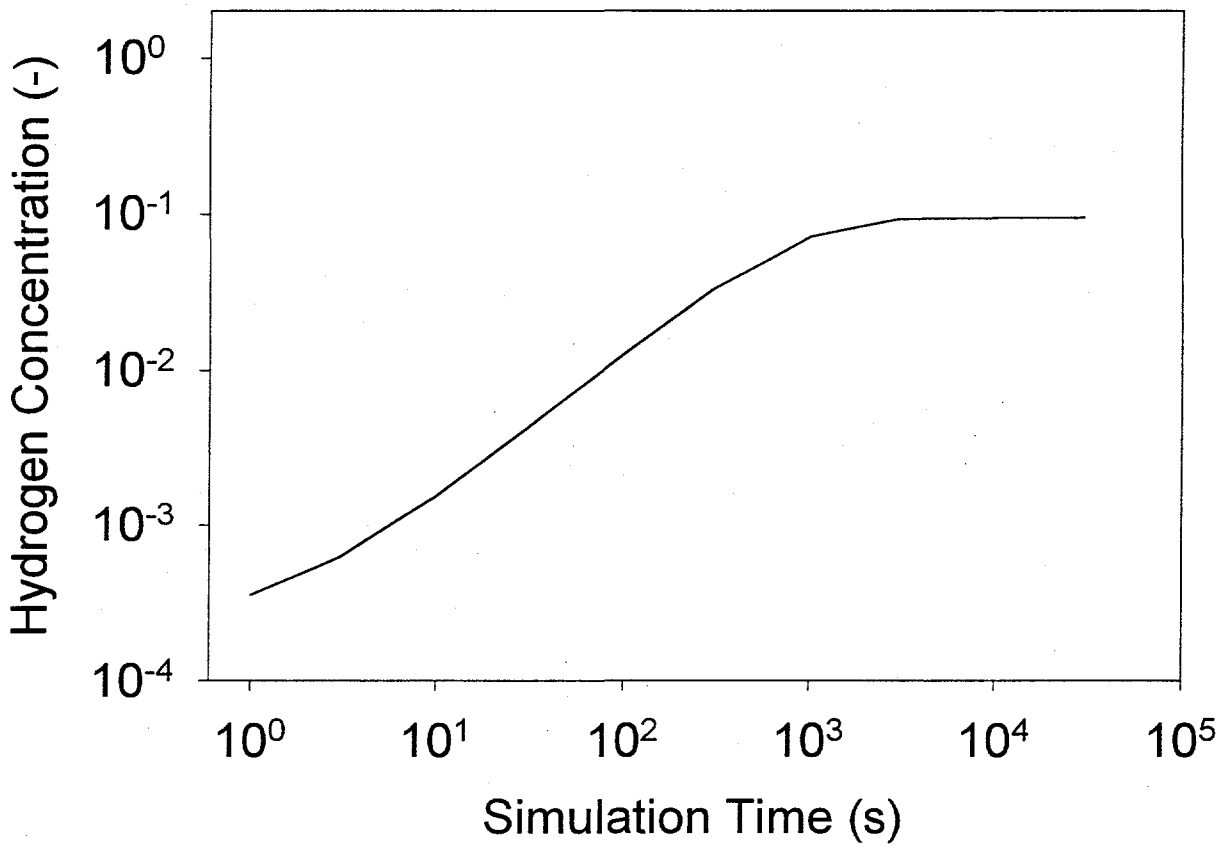

Fig. 4. Time evolution of grain boundary hydrogen content for a clean grain boundary during aging of pre-charged samples. The simulation is performed without outgassing.

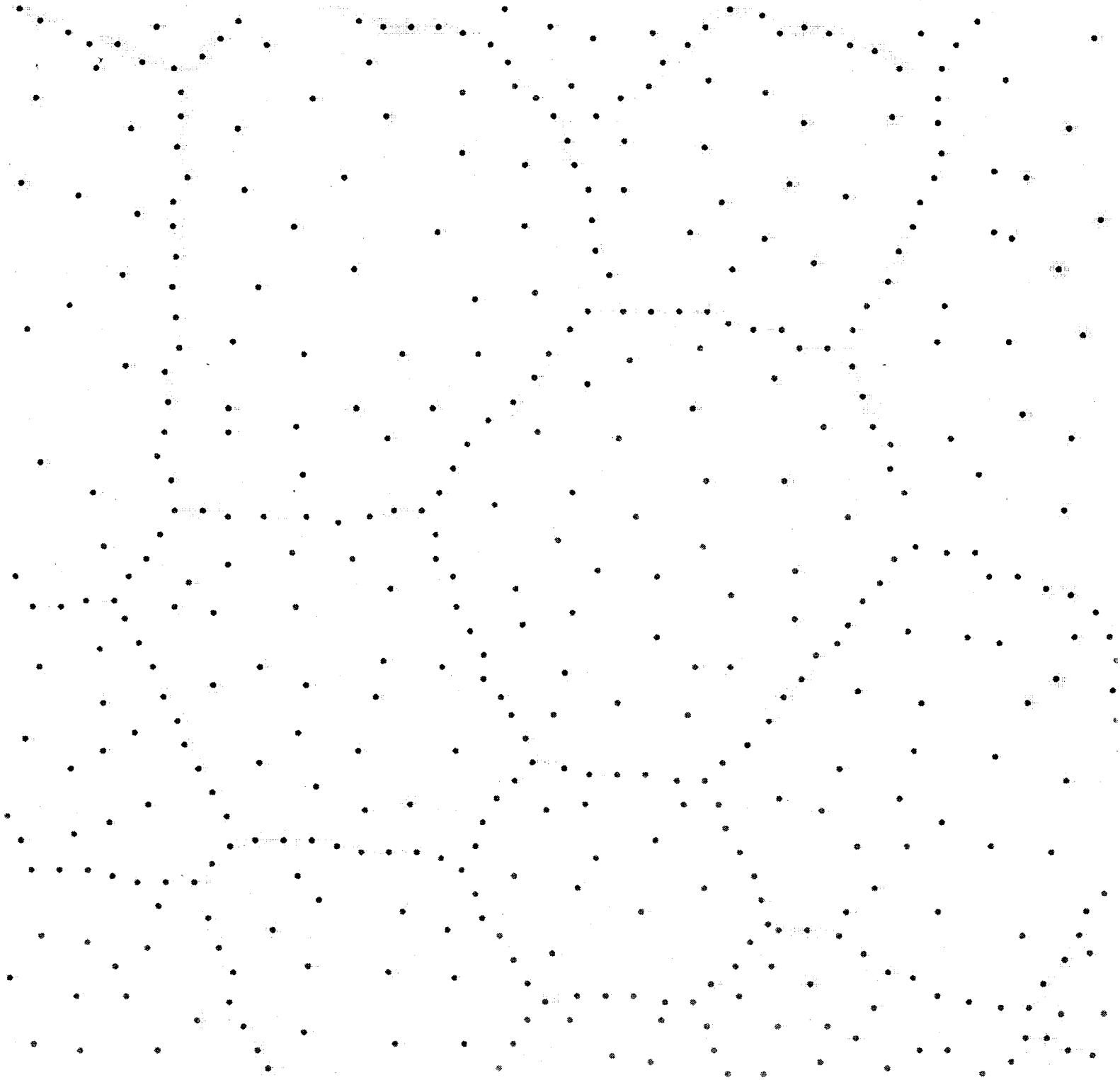

Fig. 5. Equilibrium concentration of hydrogen at each node in one of the samples containing both intergranular and transgranular carbide particles. The darkest nodes represent grain boundary hydrogen content of about 10^6 appm. Grey represents a value near 10^5 appm.

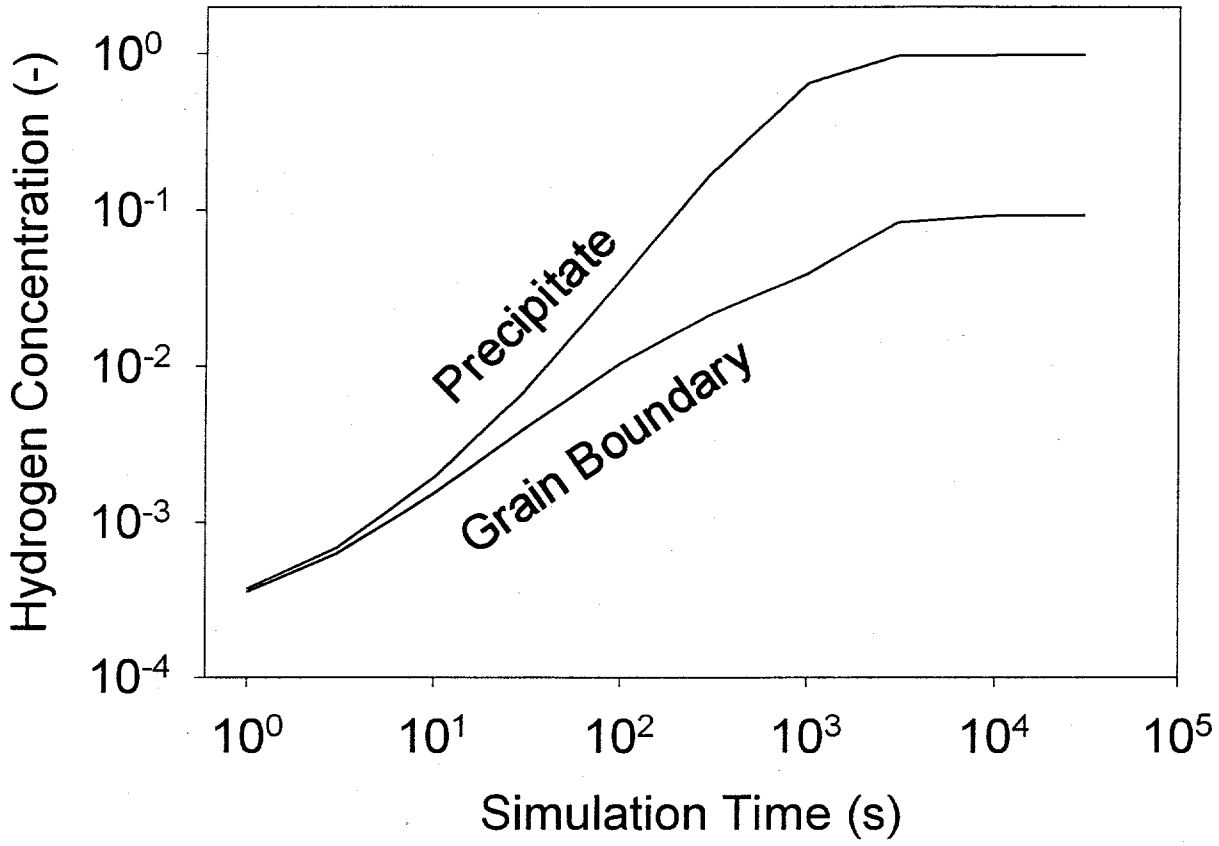

Fig. 6. Time evolution of grain boundary hydrogen content (away from precipitates) and precipitate-matrix interface hydrogen content for sample containing intergranular precipitates.

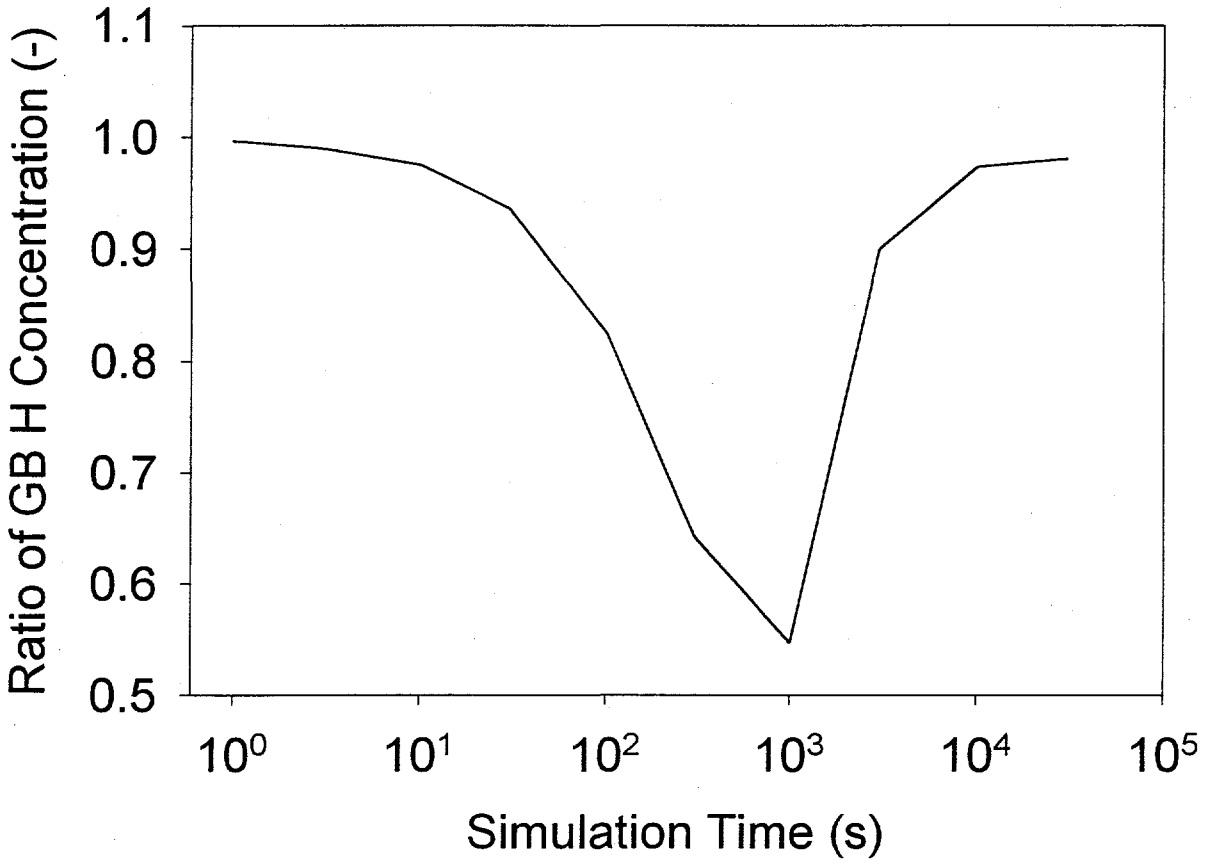

Fig. 7. Time evolution of the ratio of grain boundary hydrogen content for samples in the presence and absence of intergranular carbides. Carbides suppress the buildup of grain boundary hydrogen in these simulations.

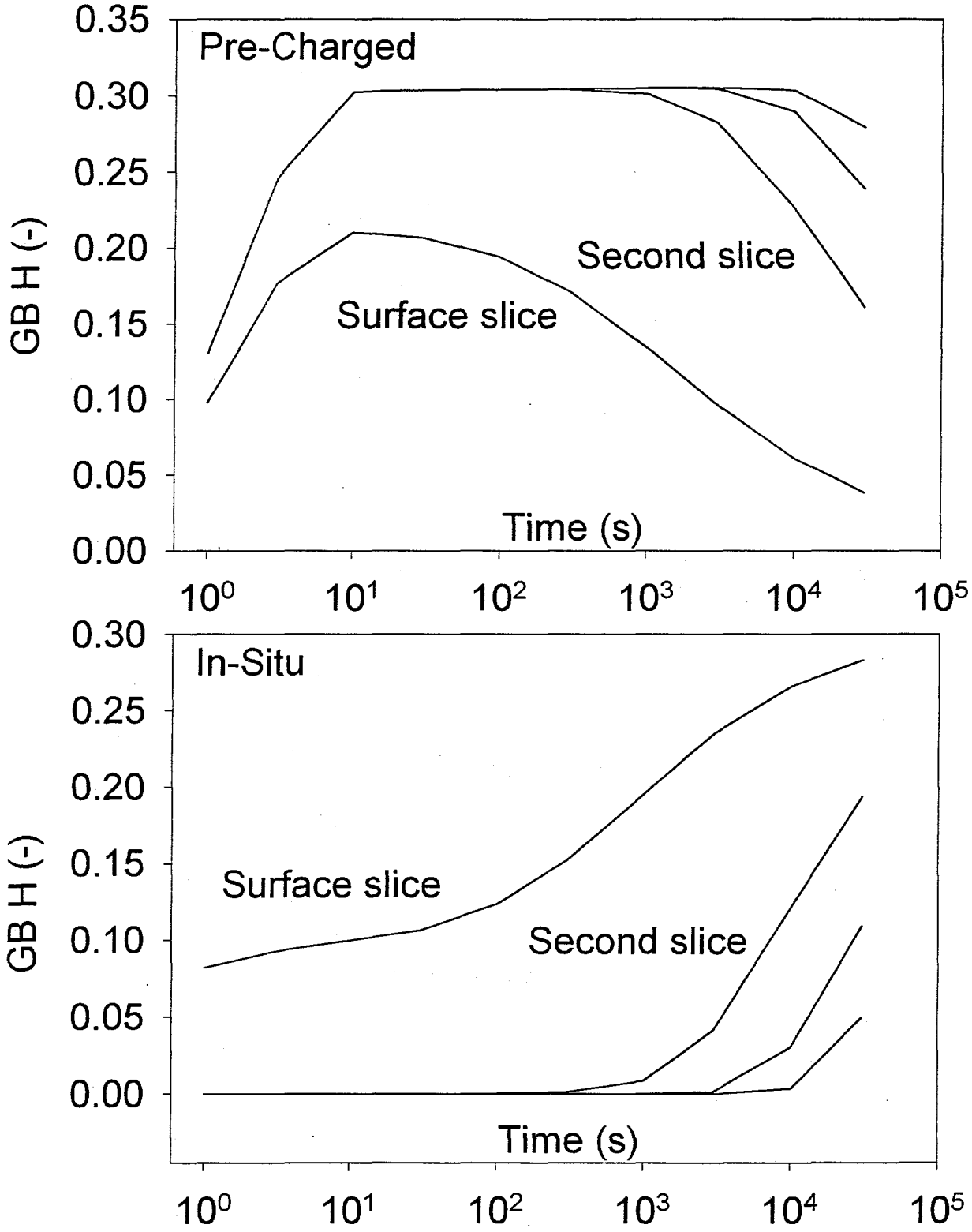

Fig. 8. Time evolution of grain boundary hydrogen content for pre-charged sample and in-situ sample as a function of distance from the free surface. Each curve represents an average for a 50 μm wide slice.

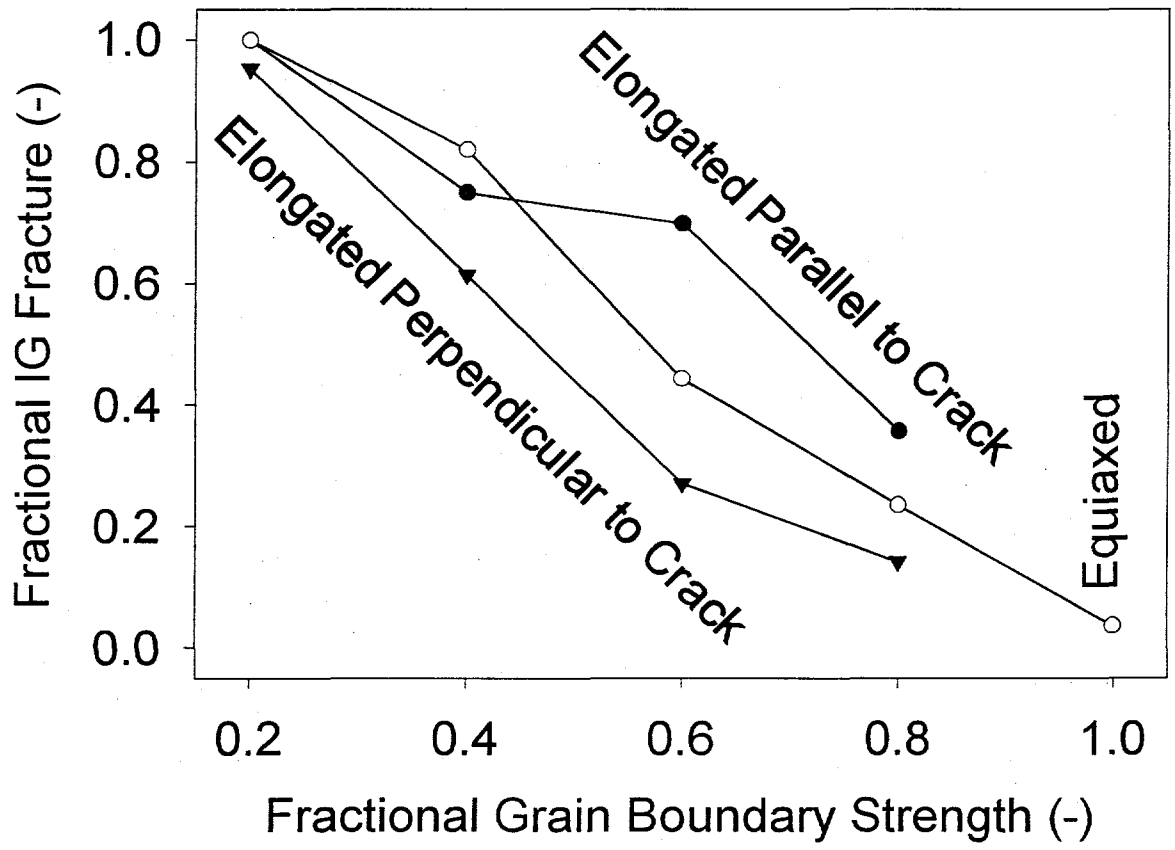

Fig. 9. Fractional intergranular failure (number of broken grain boundary bonds / total number of broken bonds anywhere in the sample) as a function of relative grain boundary bond strength and grain elongation. Each point is averaged from 2 simulations.

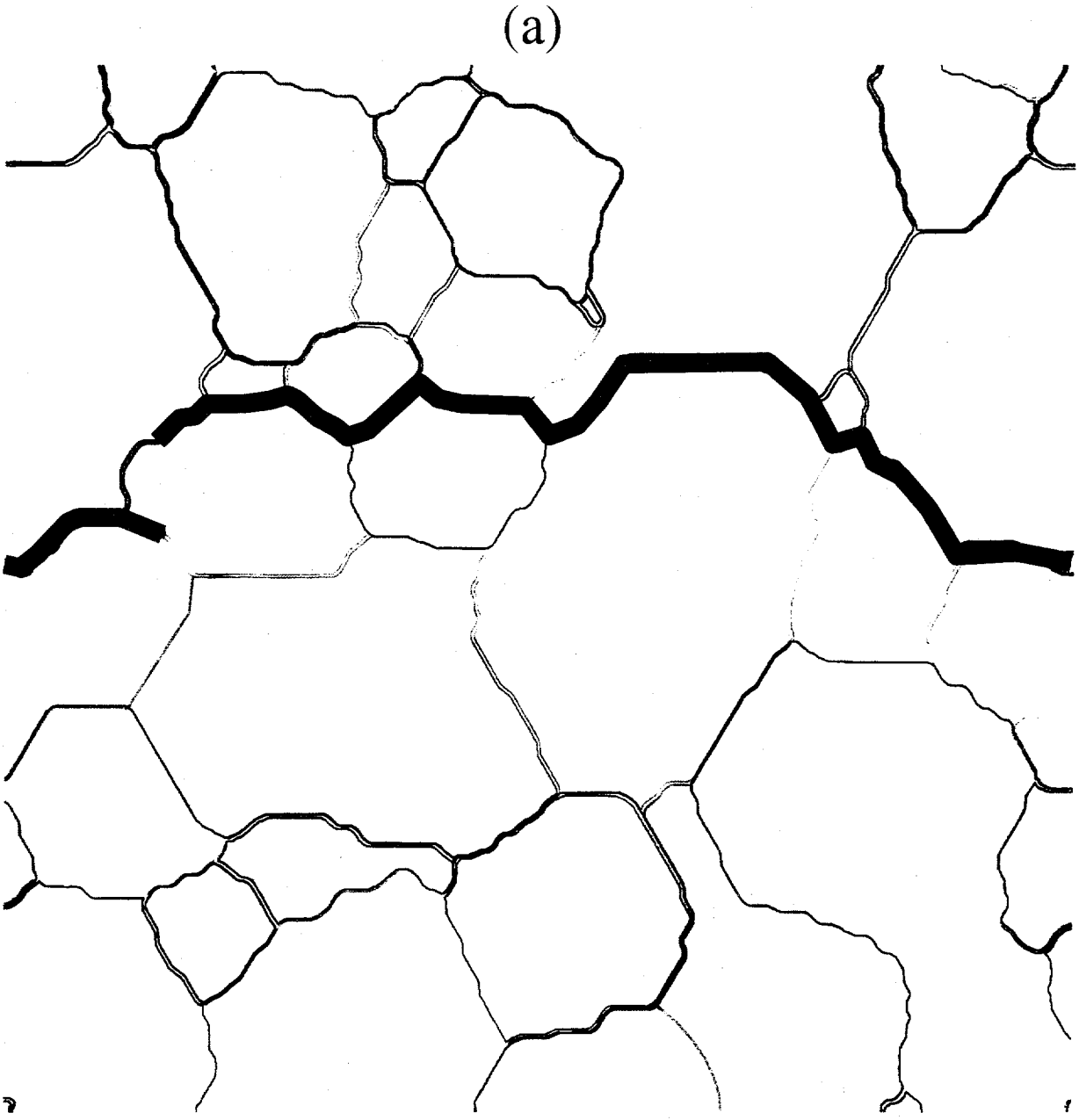

Fig. 10a. Crack morphology at the end of the simulation for equiaxed sample A with 20% grain boundary bond strength. The crack path is largely intergranular.

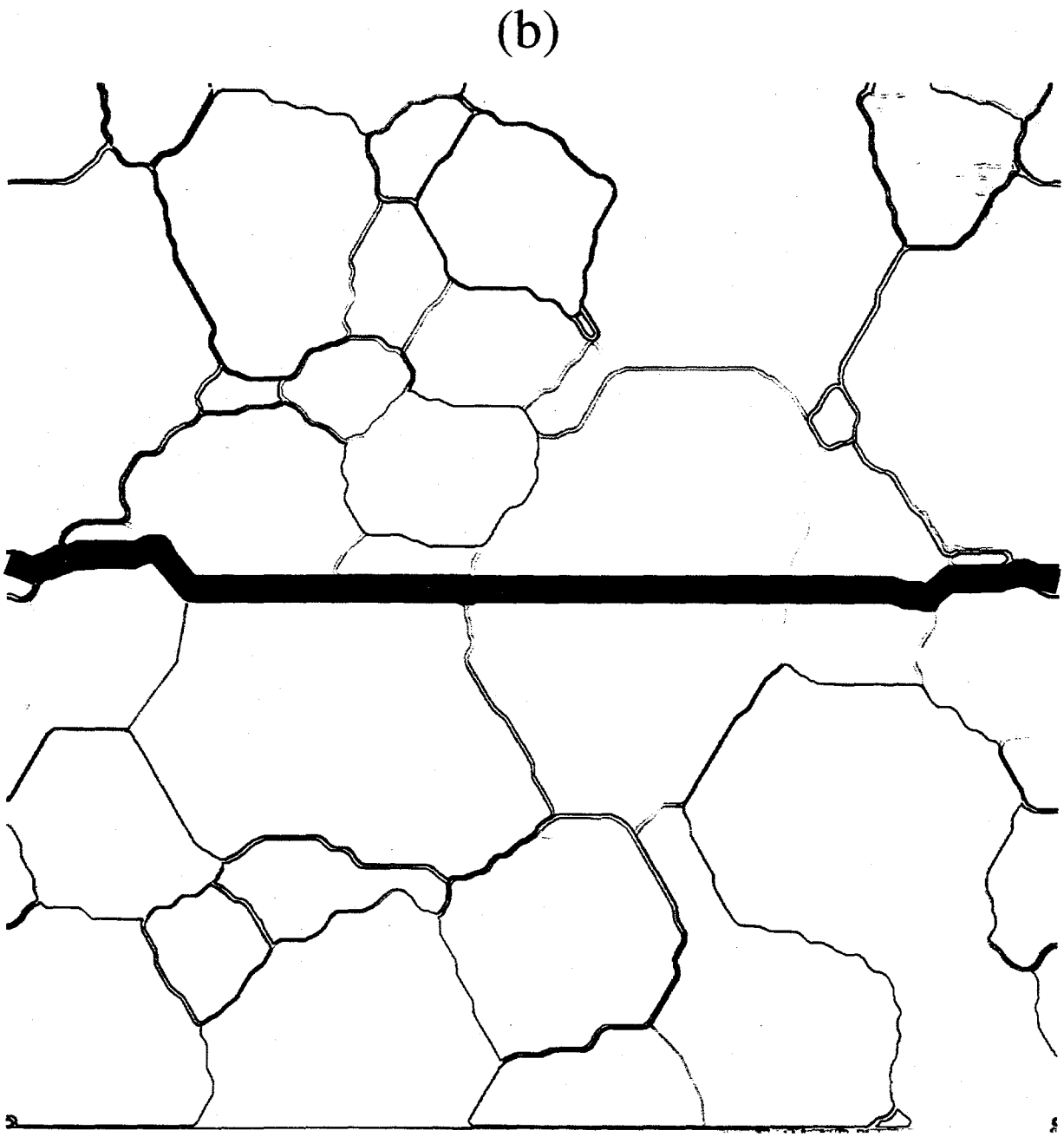

Fig. 10b. Crack morphology at the end of the simulation for equiaxed sample A with 80% grain boundary bond strength. The crack path is largely transgranular.

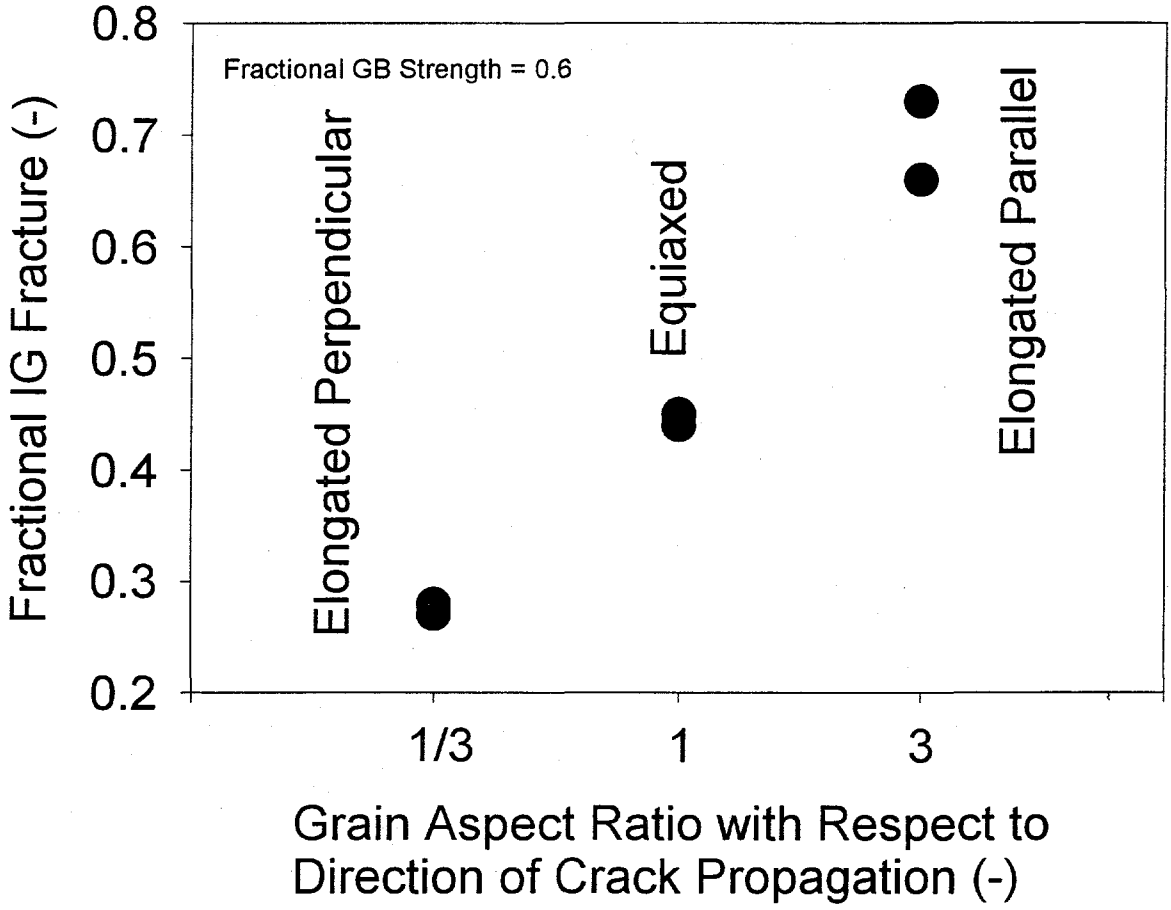

Fig. 11. Fractional integranular failure (number of broken grain boundary bonds / total number of broken bonds anywhere in the sample) as a function of grain orientation for grain boundary bond strength of 60%.

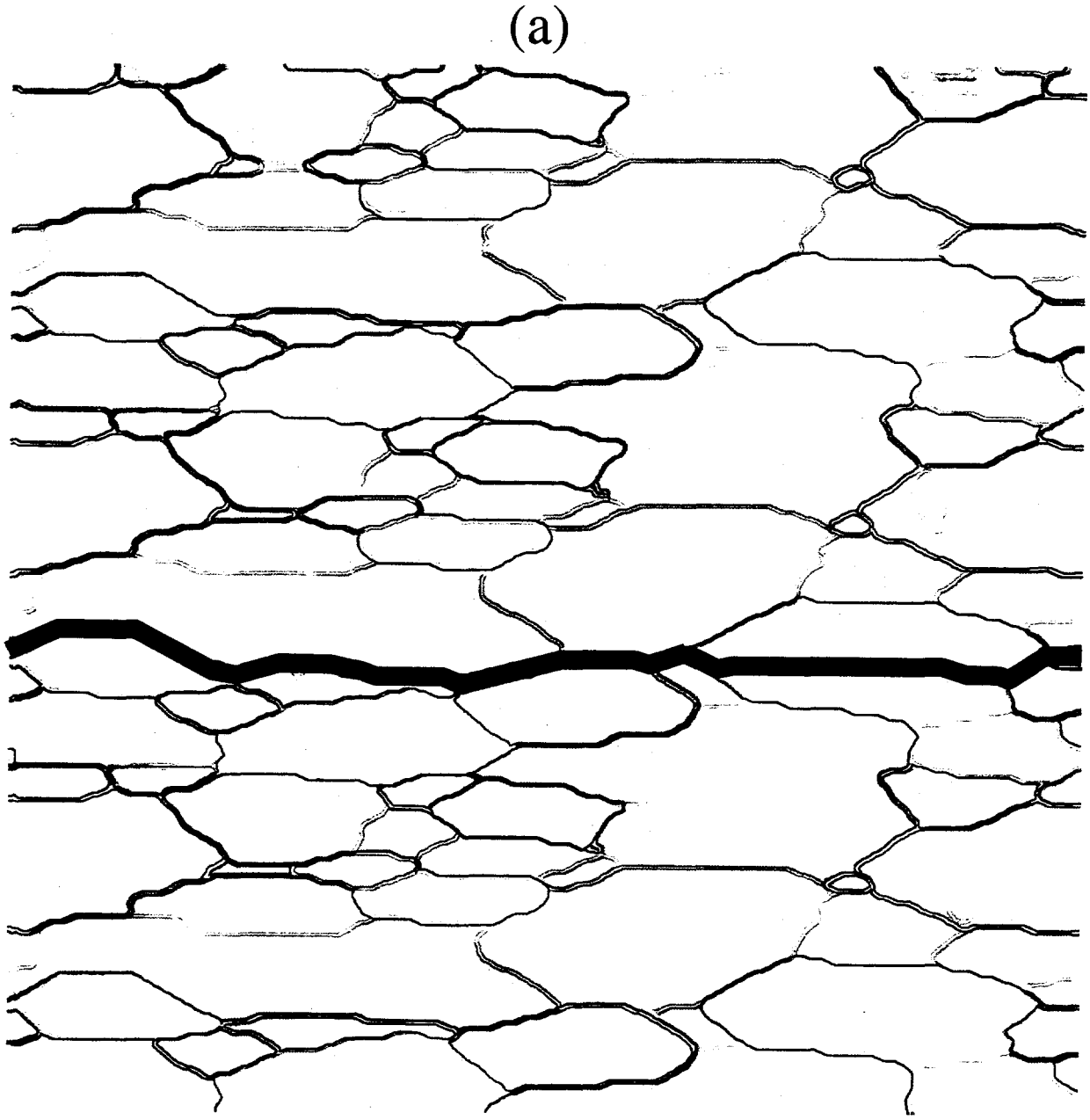

Fig. 12a. Crack morphology at the end of the simulation for sample Ax (grains elongated parallel to crack propagation) with 60% grain boundary bond strength. The crack path is largely intergranular.

(b)

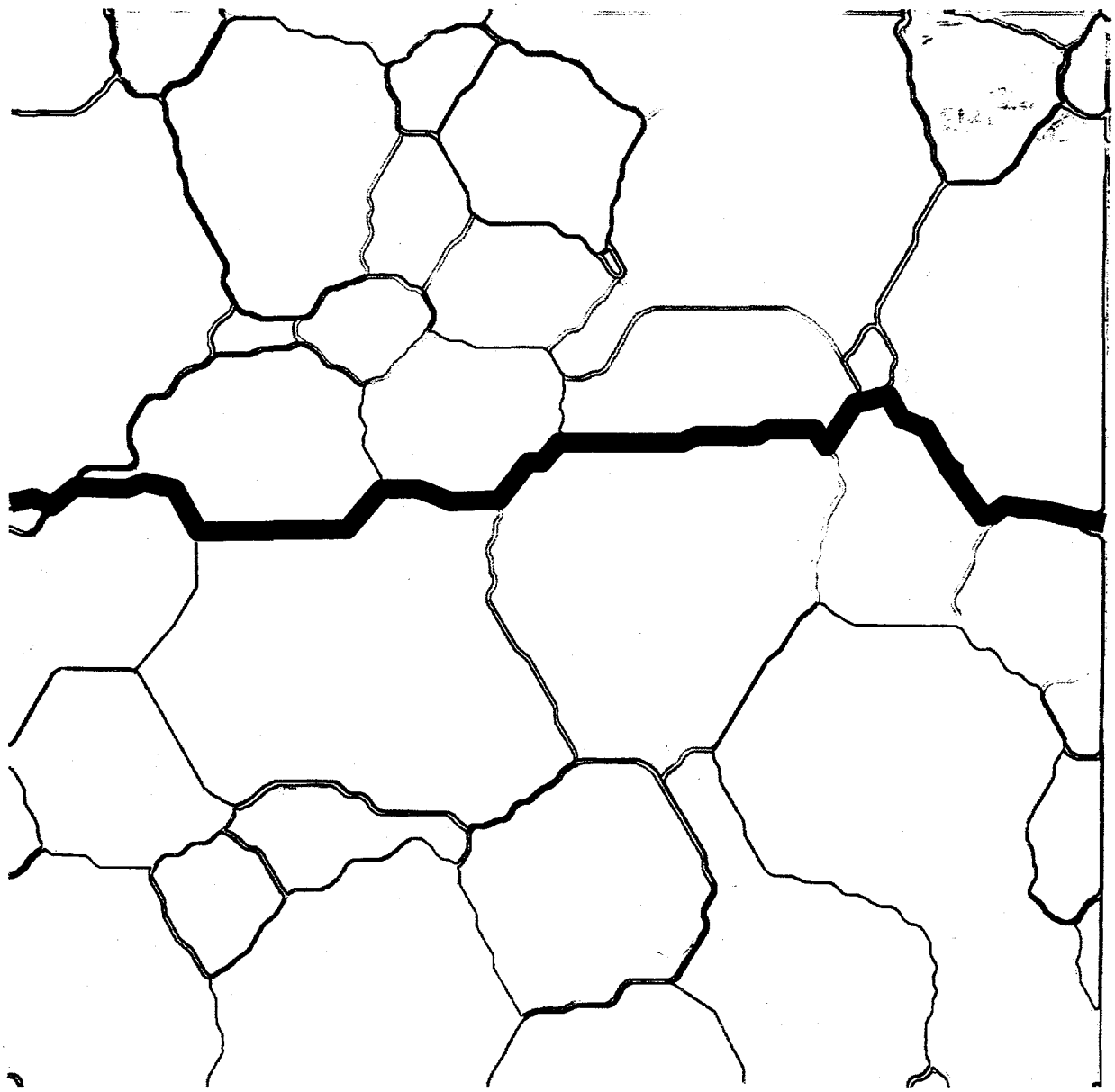

Fig. 12b. Crack morphology at the end of the simulation for sample A (equiaxed grains) with 60% grain boundary bond strength. The crack path is intergranular and transgranular.

(c)

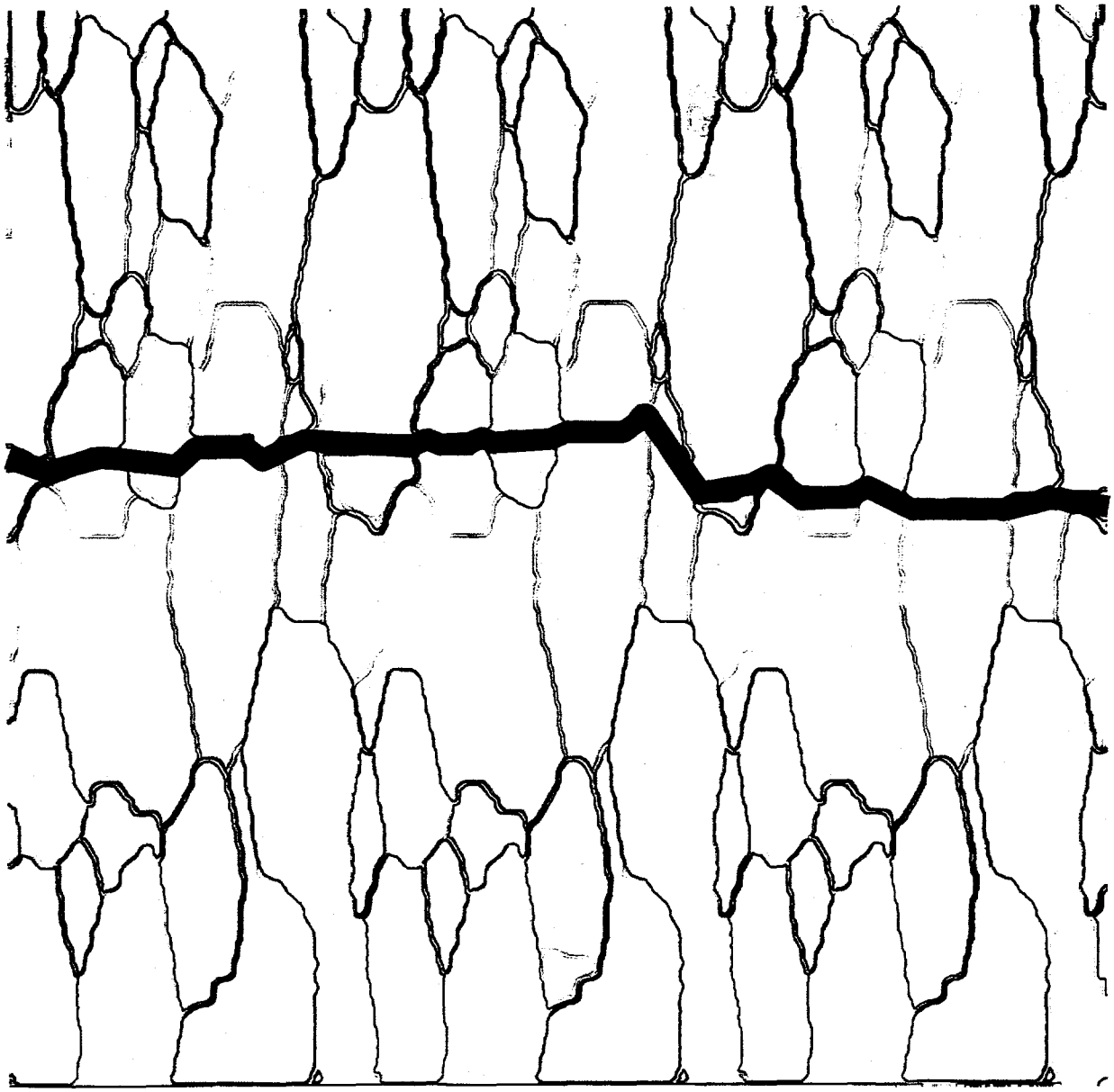

Fig. 12c. Crack morphology at the end of the simulation for sample Ay (grains elongated perpendicular to crack propagation) with 60% grain boundary bond strength. The crack path is largely transgranular.

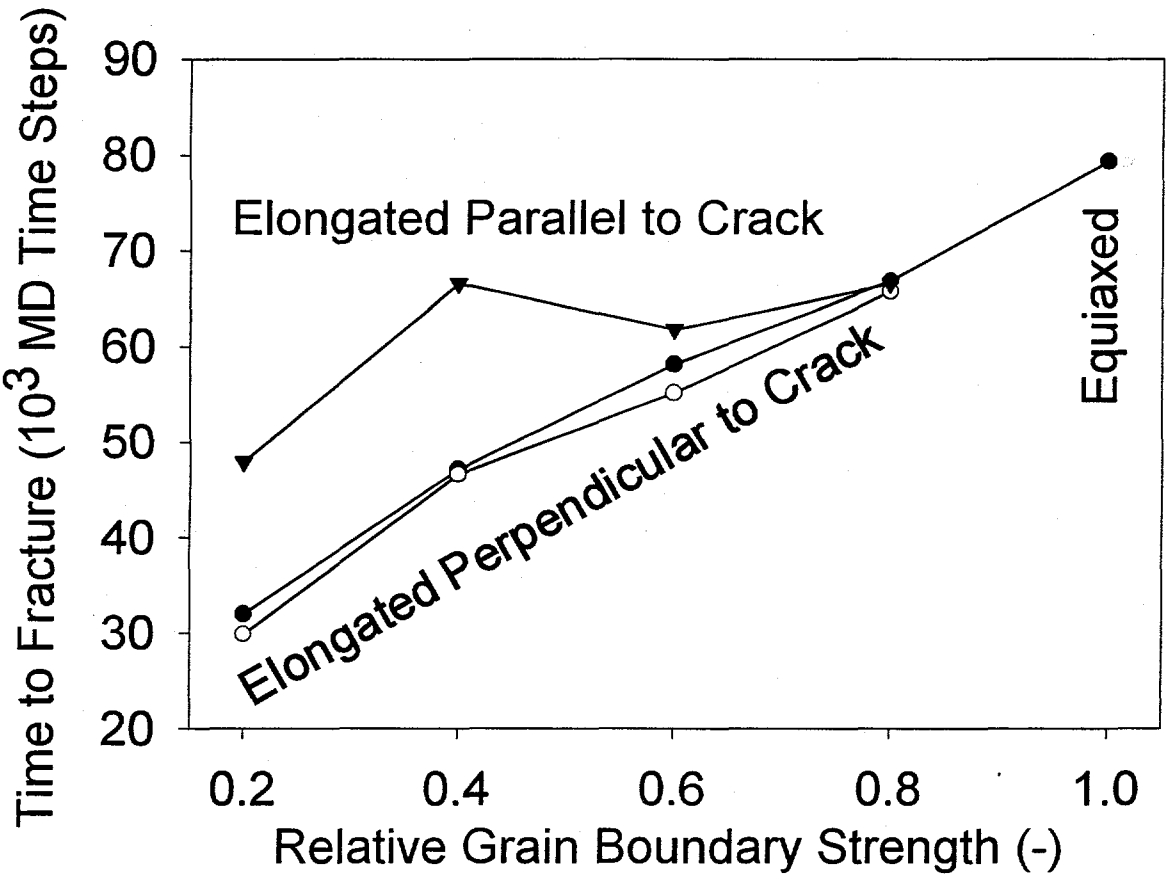

Fig. 13. Time to failure (crack extends across the entire thickness of the sample) as a function of relative grain boundary bond strength and grain elongation. Each point is averaged from 2 simulations.

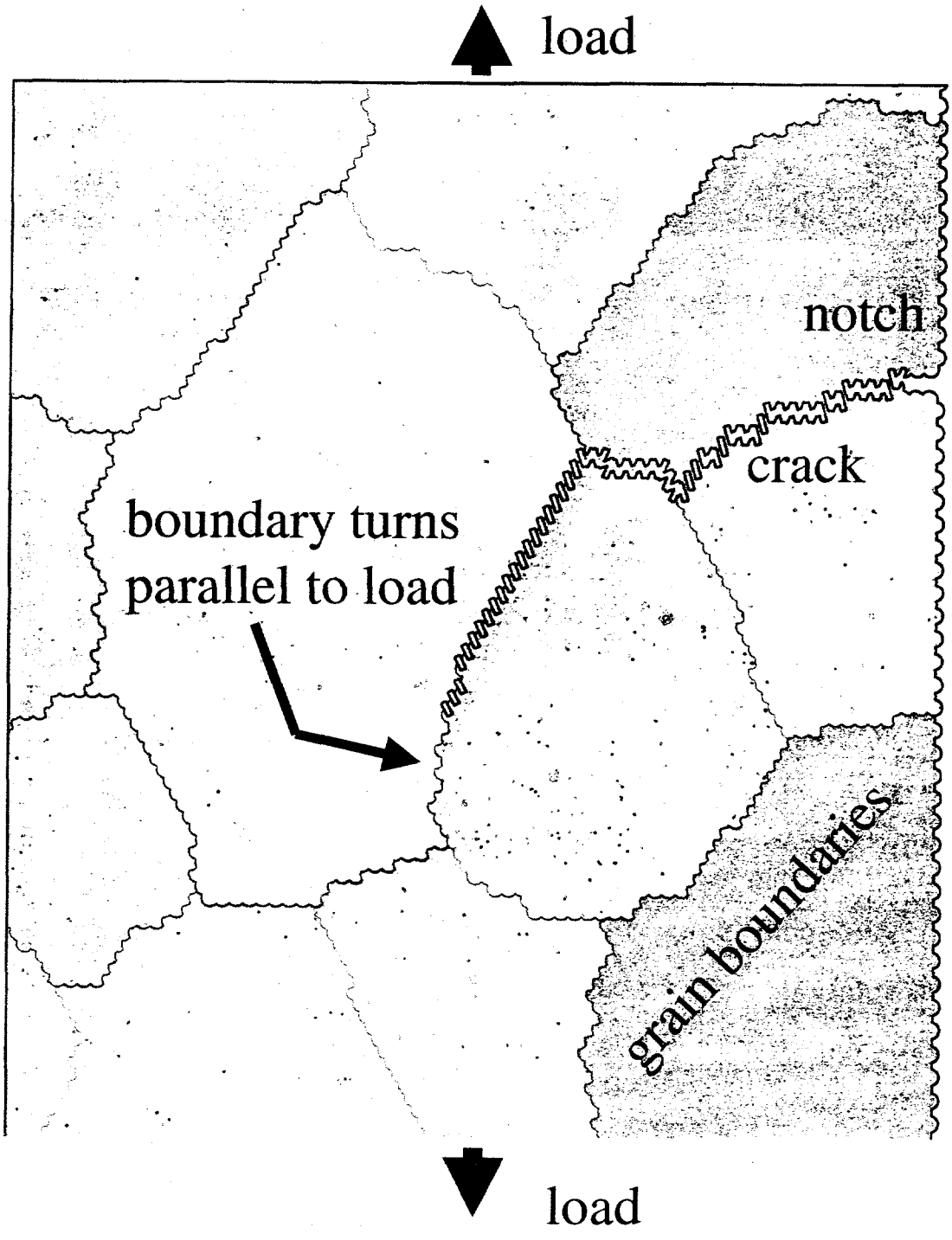

Fig. 14. Portion of sample B finite mesh showing broken bonds at 22000 time steps. The crack has propagated in from the right and down the grain boundary, but halts temporarily as the boundary turns downward, taking the boundary bonds out of a high strain orientation.

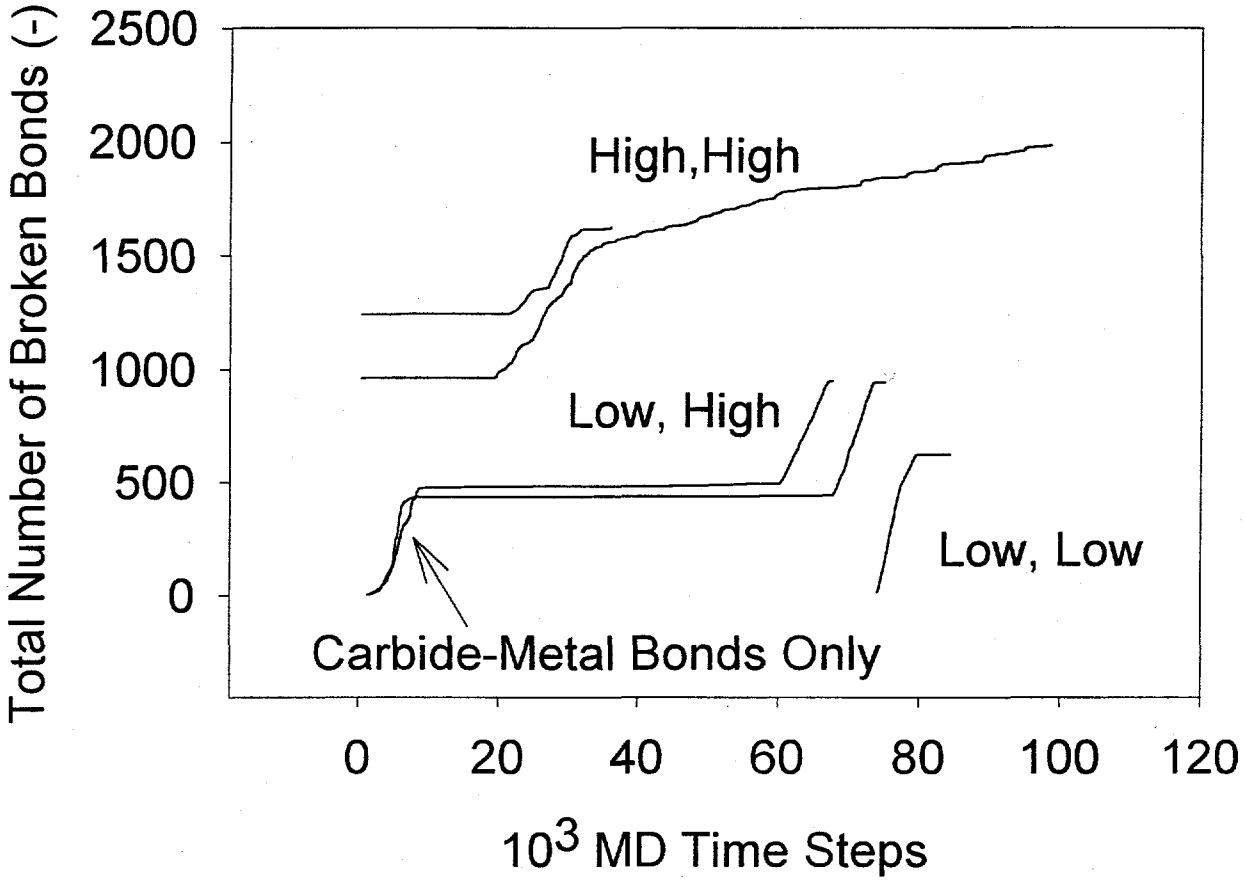

Fig. 15. Time evolution of the number of broken bonds for sample containing intergranular carbides.

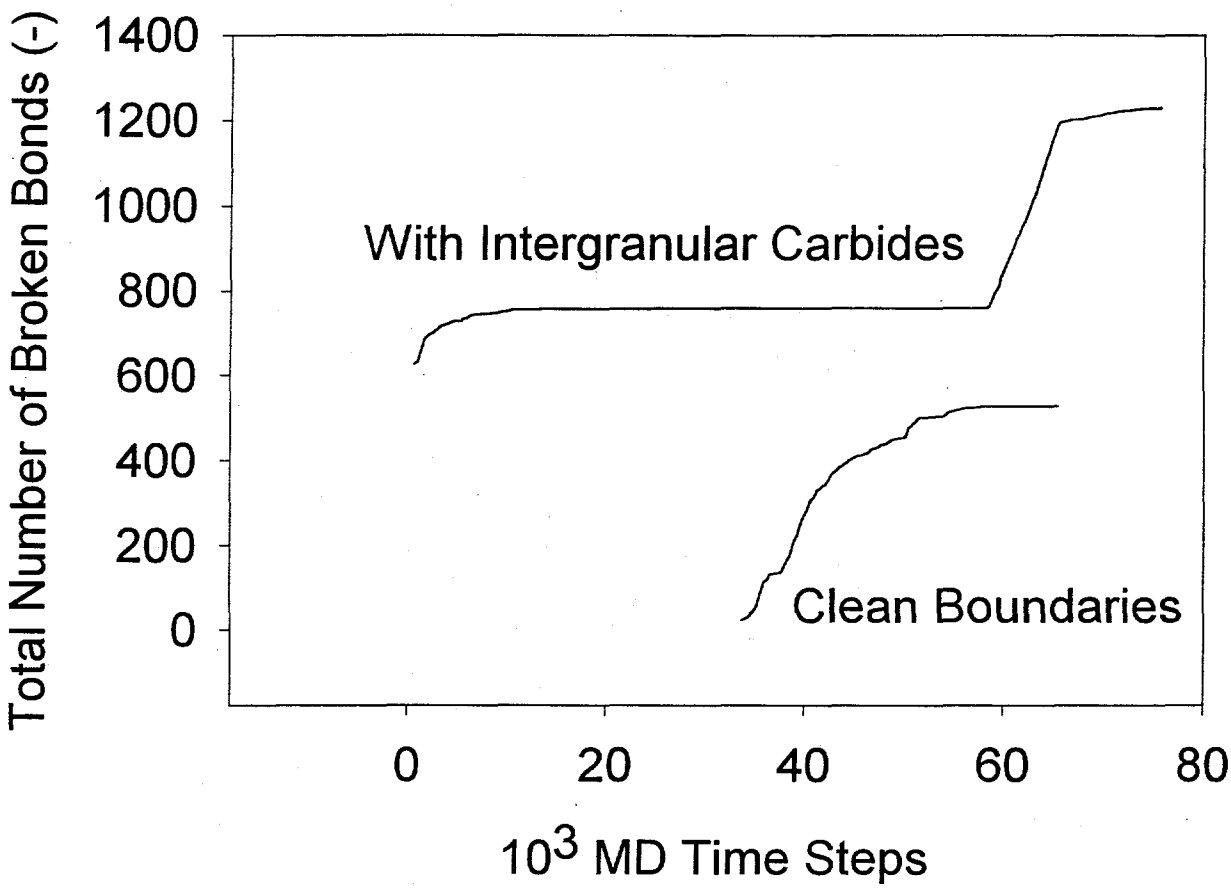

Fig. 16. Time evolution of the number of broken bonds for samples aged to 1000 seconds with and without intergranular carbides.

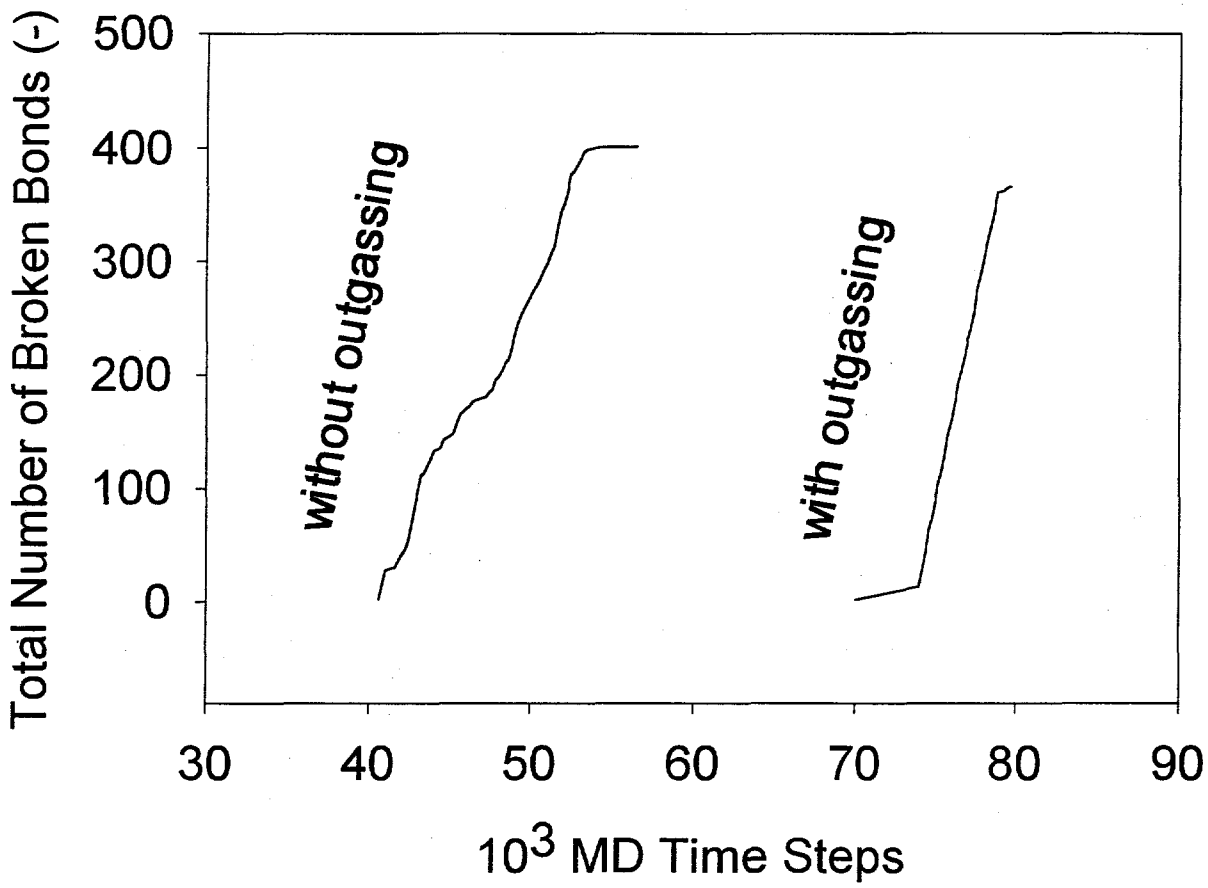

Fig. 17. Time evolution of the number of broken bonds for aged samples with and without surface outgassing.